GFZ
Helmholtz-Zentrum
POTSDAM

Originally published as:

Upper-mantle *P*- and *S*-wave velocities across the Northern Tornquist Zone from traveltime tomography

Babak Hejrani,[1,*] Niels Balling,[1] Bo Holm Jacobsen[1] and Frederik Tilmann[2]

[1]*Department of Geoscience, Aarhus University, Aarhus, Denmark. E-mail:* babak.hejrani@anu.edu.au
[2]*GFZ, German Research Centre for Geosciences, Potsdam, Germany*

SUMMARY

This study presents *P*- and *S*-wave velocity variations for the upper mantle in southern Scandinavia and northern Germany based on teleseismic traveltime tomography. Tectonically, this region includes the entire northern part of the prominent Tornquist Zone which follows along the transition from old Precambrian shield units to the east to younger Phanerozoic deep sedimentary basins to the southwest. We combine data from several separate temporary arrays/profiles (276 stations) deployed over a period of about 15 yr and permanent networks (31 stations) covering the areas of Denmark, northern Germany, southern Sweden and southern Norway. By performing an integrated *P*- and *S*-traveltime analysis, we obtain the first high-resolution combined 3-D V_P and V_S models, including variations in the V_P/V_S ratio, for the whole of this region of study. Relative station mean traveltime residuals vary within ± 1 s for *P* wave and ± 2 s for *S* wave, with early arrivals in shield areas of southern Sweden and later arrivals in the Danish and North German Basins, as well as in most of southern Norway. In good accordance with previous, mainly *P*-velocity models, a marked upper-mantle velocity boundary (UMVB) is accurately delineated between shield areas (with high seismic mantle velocity) and basins (with lower velocity). It continues northwards into southern Norway near the Oslo Graben area and further north across the Southern Scandes Mountains. This main boundary, extending to a depth of at least 300 km, is even more pronounced in our new *S*-velocity model, with velocity contrasts of up to ± 2–3 per cent. It is also clearly reflected in the V_P/V_S ratio. Differences in this ratio of up to about ± 2 per cent are observed across the boundary, with generally low values in shield areas to the east and relatively higher values in basin areas to the southwest and in most of southern Norway. Differences in the V_P/V_S ratio are believed to be a rather robust indicator of upper-mantle compositional differences. For the depth interval of about 100–300 km, thick, depleted, relatively cold shield lithosphere is indicated in southern Sweden, contrasting with more fertile, warm mantle asthenosphere beneath most of the basins in Denmark and northern Germany. Both compositional and temperature differences seem to play a significant role in explaining the UMVB between southern Norway and southern Sweden. In addition to the main regional upper-mantle velocity contrasts, a number of more local anomaly features are also outlined and discussed.

Key words: Body waves; Seismic tomography; Cratons; Dynamics of lithosphere and mantle; Europe.

INTRODUCTION AND TECTONIC OUTLINE

The European continent is divided into an old and a younger part by the northwest-southeast trending Tornquist/Trans-European Suture Zone, which extends from the Black Sea to the North Sea. It separates the East European Craton with Archean and Proterozoic lithosphere from the younger terranes accreted during the Phanerozoic that form Central and Western Europe (Gee & Stephenson 2006). These major tectonic units are characterized by significant differences in structural and physical properties such as crustal structure, deep seismic velocity and heat flow (Zielhuis & Nolet 1994; Artemieva *et al.* 2006; Artemieva & Thybo 2013). Low heat flow, thick crust and thick lithosphere are observed in the old craton

*Now at: Research School of Earth Science, Australian National University, ACT, Australia.
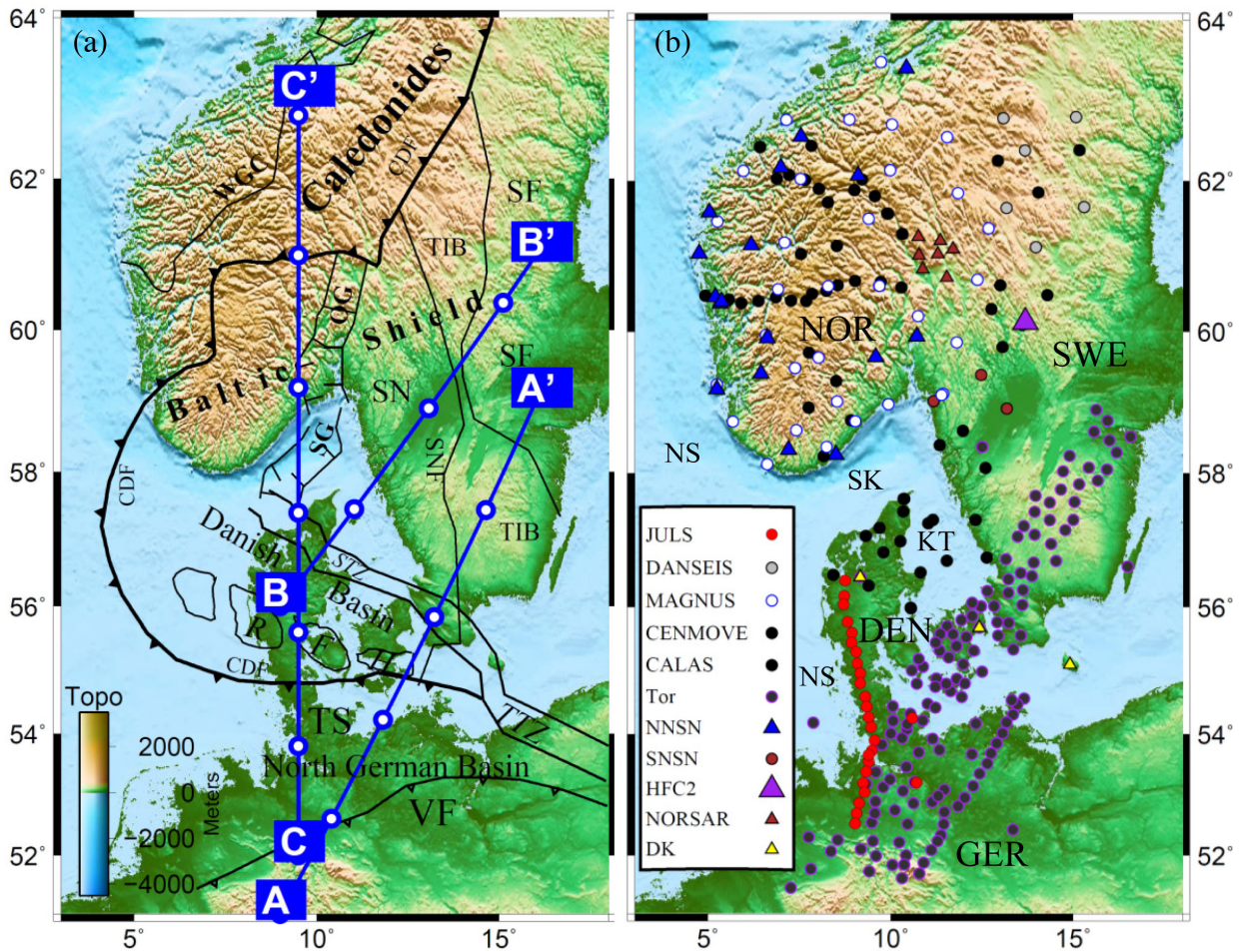
Figure 1. Structural and topographic maps of the study area with seismological stations. (a) Structural setting and location of three vertical sections, AA′, BB′ and CC′ for which seismic velocity results are shown in Fig. 8. Circle marks along the profiles are indicated at 200 km intervals. CDF, Caledonian Deformation Front; OG, Oslo Graben; RFH, Ringkøbing-Fyn High; SG, Skagerak Graben; SN, Sveconorwegian; SNF, Sveconorwegian Front; SF, Svecofennian; STZ, Sorgenfrei-Tornquist Zone; TIB, Trans-Scandinavian Igneous Belt; TS, Thor suture; TTZ, Teisseyre-Tornquist Zone; VF, Variscan Front; WGC, Western Gneiss Complex. (b) Locations of applied seismological stations; triangle for permanent and circle for temporary stations with different colours indicating separate arrays/profiles. Main geographic items are also indicated: DEN, Denmark; GER, Germany; KT, Kattegat; NOR, Norway; NS, North Sea; SK, Skagerrak; SWE, Sweden.

to the east and north, in marked contrast to generally higher heat flow, thinner crust and thinner lithosphere in most of Central and Western Europe. The focus of this study is the variation of seismic velocities (*P* waves and *S* waves) in the upper mantle across the northern part of the Tornquist Zone in Southern Scandinavia and Northern Germany and its geodynamic implications.

The main structural and tectonic units in the study area are the Baltic Shield (mainly southern Sweden), the Caledonides (southern Norway) and the Danish and North German Basins (Fig. 1a). There is a general younging of tectonic units from the Svecofennian (1.9–1.8 Ga) shield units to the northeast, over the Precambrian units in the southwestern part of the shield, formed about 1.65–1.5 Ga ago with significant reworking during the 1.15–0.9 Ga old Sveconorwegian orogeny, to the Palaeozoic and Mesozoic sedimentary basins to the southwest. The shield units constitute the western part of the palaeo-continent Baltica. For recent reviews of the formation and evolution of this continent and its southwestern margins we refer to Bogdanova *et al.* (2008) and Bingen *et al.* (2008a,b).

Precambrian crust extends to the southwest beneath the Danish Basin down to the Thor Suture (Fig. 1a; part of the Trans-

European Suture Zone, also referred to as the Tornquist Suture) formed by the collision/docking of Baltica with the micro-continent Avalonia around the Ordovician-Silurian boundary (c. 440 Ma, Cocks & Torsvik 2006). This collision was followed by that of Baltica/Avalonia with Laurentia which resulted in formation of the large-scale Caledonian Mountain Range, including the c. 430–390 Ma old Scandinavian Caledonides (Roberts 2003; Cocks & Torsvik 2006).

The southwestern part of the study area (Danish, North German and adjacent North Sea areas) was subject to significant Late Carboniferous-Permian magmatic and tectonic activity (e.g. Heeremans & Faleide 2004) which, according to Torsvik *et al.* (2008), have the characteristics of a Large Igneous Province (LIP) centred on the Skagerrak Sea (Skagerrak-Centered LIP: SCLIP). Both the Danish Basin and the North German Basin were initiated in relation to these magmatic and tectonic events. Lithospheric stretching in the thermally weakened crust–upper-mantle formed an important basin-generating mechanism leading to deep sedimentary basins (Van Wees *et al.* 2000; Frederiksen *et al.* 2001; Scheck-Wenderoth & Lamarche 2005; McCann *et al.* 2006). The

Oslo-Skagerrak rift and graben system were also formed as part of these events. During the Mesozoic and the Cenozoic, the southwestern areas experienced rifting and subsidence offshore Norway, doming in the central North Sea (Mid-Jurassic) and finally the Palaeocene (c. 55 Ma) opening of the North Atlantic.

The age and origin of high topography of the Scandinavian Mountains (the Scandes) are a matter of debate. A widely held view has been that the high topography is relatively young, with a main uplift phase during the Cenozoic (e.g. Dore 1992; Stuevold & Eldholm 1996; Japsen & Chalmers 2000; Lidmar-Bergstrom *et al.* 2000; Bonow *et al.* 2007; Green *et al.* 2013). Recently, Nielsen *et al.* (2009, 2010) argued that the present high topography is mainly a long-lived remnant of the Caledonian Mountains. This view has generated some debate (Chalmers *et al.* 2010; Nielsen *et al.* 2010).

A main tectonic and deep structural boundary in our study area is defined by the transition from old shield units to deep basins along and east of the Sorgenfrei–Tornquist Zone (STZ, eastern Denmark and southwestern Sweden) and along the Teisseyre–Tornquist Zone (TTZ, northern Poland and northeastern Germany) (Fig. 1a; Medhus *et al.* 2012a). These zones are here collectively and informally referred to as the Northern Tornquist Zone. The STZ is a marked structural lineament within the Precambrian Baltica crust and defined in EUGENO-S Working Group (1988) along the trend of Late Cretaceous-Tertiary inversion tectonics. We emphasize that the boundary between Baltica crust and Avalonia/Caledonian crust is not along the STZ but further to the southwest along the Thor Suture, close to the Caledonian Deformation Front (Fig. 1a) (*cf.* Abramovitz & Thybo 2000; Balling 2000; Torsvik & Rehnström 2003).

Our study area is almost the same as that covered by *P*-velocity models in Medhus *et al.* (2012a). We include new data (in particular JULS project data in the southwestern part, Fig. 1b), and present results of an integrated relative traveltime tomography study giving information of *P*-wave velocity, *S*-wave velocity and the V_P/V_S ratio. High-resolution information on this ratio for this region is presented here for the first time. This allows a better understanding of the role of compositional differences, in addition to temperature differences, in explaining significant variations in the upper-mantle velocity. In this study, we present high-resolution 3-D seismic velocity models for the upper mantle across the region of southern Scandinavia and main tectonic units, as outlined above.

Previous studies

The study area is generally quite well covered with geophysical investigations to provide information about the structure of the crust and upper mantle. Crustal velocity and thickness are mainly determined by seismic refraction experiments and by analyses of receiver functions (EUGENO-S Working Group 1988; Iwasaki *et al.* 1994; Svenningsen *et al.* 2007; Olsson *et al.* 2008; Sandrin & Thybo 2008; Stratford *et al.* 2009; Stratford & Thybo 2011; England & Ebbing 2012). For a recent compilation and analysis, see Artemieva & Thybo (2013). The typical thickness of shield crust in southern Sweden is around 45 km (range about 40–50 km), which contrasts with the significantly thinner crust of about 30 km across the Danish and North German Basins. Crustal thickness increases from about 30 km along the Norwegian west coast to about 40 km beneath areas of high topography below the Scandes Mountains. This increase in crustal thickness is associated with a decrease in Bouguer gravity from close to zero in coastal areas to around −100 mGal in areas of high topography (Balling 1980; Ebbing *et al.* 2012). The deeper

parts of shield crust are characterized by relatively high *P*-wave velocity (>7 km s^{-1}) (*cf.* Artemieva & Thybo 2013) and high density (Ebbing *et al.* 2012).

Several studies have shown the existence of distinct contrasts in seismic velocities in the upper mantle of the study area, with generally high velocity to the east beneath shield areas in Sweden and lower velocities beneath sedimentary basins to the southwest, as well as in most of southern Norway. The first high-resolution study to outline a significant velocity contrast in this area was the teleseismic Tor project with information on seismic velocity contrasts across the southeastern part of the STZ (*cf.* Gregersen *et al.* 2002, 2010 for reviews). Medhus *et al.* (2012a), using *P*-wave teleseismic traveltime tomography covering most of the present study area, showed that the boundary between upper mantle with high and low velocities extends to the north-northwest close to the STZ in the Kattegat area between Denmark and Sweden, but then deviates from the STZ (which continues to the northwest into northernmost Denmark and the Danish Basin, *cf.* Fig. 1a) by running north into southern Norway near the Oslo Graben. That study also outlined a *P*-wave low-velocity uppermost mantle below most of southern Norway, an area also characterized by low *S*-wave velocities, as shown by both *S*-wave traveltime tomography (Wawerzinek *et al.* 2013) and surface wave analysis (Weidle & Maupin 2008; Maupin 2011; Köhler *et al.* 2012). The above studies with results for southern Norway included data from the MAGNUS project (Weidle *et al.* 2010) and formed part of the TopoScandiaDeep project (for a review see Maupin *et al.* 2013), a component of the TOPOEUROPE program. Some recent continent-scale models also show velocity contrasts in southern Scandinavia for both *P* and *S* waves (Jakovlev *et al.* 2012; Zhu *et al.* 2012; Rickers *et al.* 2013), although they generally have lower resolution than the above studies. Kind *et al.* (2013) studied the upper mantle from Germany across Scandinavia to northern Sweden with seismic *S* receiver functions. Of particular interest to the present study is the interpretation of a significant increase in lithospheric thickness from Germany and Denmark (about 100 km) to further north in Scandinavia (about 200 km).

In addition to significant differences in crustal and upper-mantle structures, the study area also presents marked differences in heat flow, with generally relatively low values in the old shield and platform areas to the east (about 50–60 mW m^{-2}) in contrast to higher values (about 70–80 mW m^{-2}) in basins areas to the southwest. Southern Norway and the Scandinavian Caledonian areas show mostly intermediate values around 55–60 mW m^{-2} (Balling 1995; Slagstad *et al.* 2009). For most of the area, in particular across the STZ/TTZ, differences in heat flow seems to be associated with marked differences in depth to the lithosphere-asthenosphere boundary (Pedersen *et al.* 1994; Balling 1995; Cotte *et al.* 2002; Norden *et al.* 2008; Jones *et al.* 2010; Köhler *et al.* 2015).

DATA

We combined data from several temporary arrays/profiles run by different institutions since 1996 (Tor, CENMOVE, CALAS, MAGNUS, DANSEIS, *cf.* Medhus *et al.* 2012a) and from the new JULS project (JUtland-Lower Saxony, 2010–2012) covering southwestern Denmark and northwestern Germany. The JULS profile covers the gap between Tor and CALAS data in the German and Danish Basins and supplies the extra ray coverage to constrain 3-D tomography along the northernmost STZ. We picked arrival time data from these projects together with data from permanent stations in the region: Norwegian National Seismic Network (NNSN),

Table 1. Summary information including number of arrival time readings for seismological stations/arrays applied in this study (compare with Fig. 1b). Temporary arrays are indicated in italic.

Project/stations	Number of stations	Period of experiment/recordings	*P*-wave readings	*SV*-wave readings	*ST*-wave readings
JULS	26	2010–2012	1600	537	572
DANSEIS	6	2008–2009	689	59	73
MAGNUS	34	2006–2008	2334	962	1262
CALAS/CENMOVE	72	2002–2009	2137	716	722
Tor	138	1996–1997	2556	469	417
NNSN	16	2006–2012	918	399	468
SNSN	4	2005–2006	56	23	20
HFC2	1	2002–2012	523	183	205
NORSAR	7	2002–2009	2671	924	960
DK	3	1996–2012	857	339	368
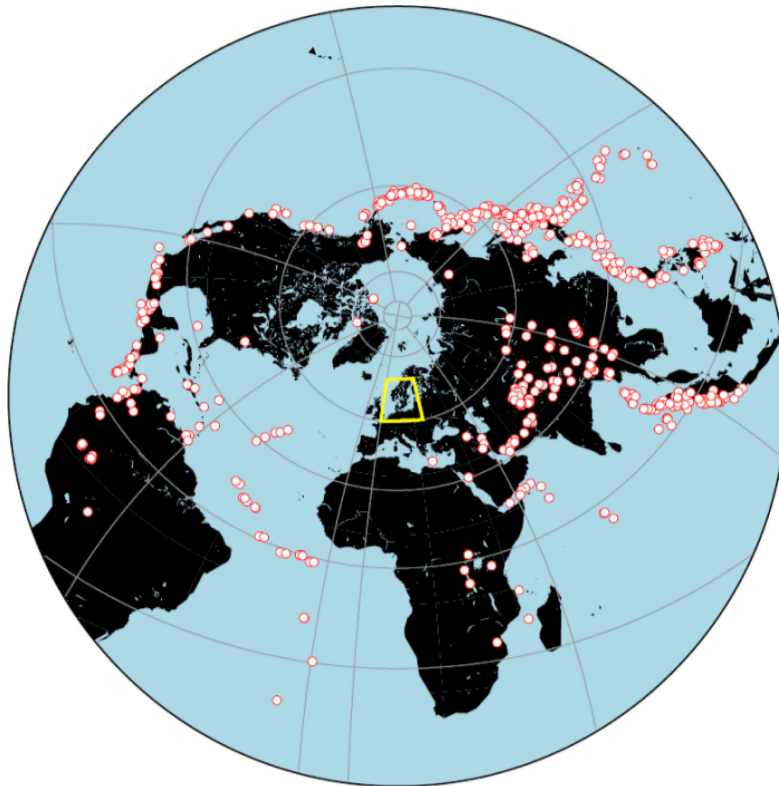
Figure 2. Location of the seismological events used in this study. The yellow frame shows the study area.

NORSAR array, Danish permanent stations (DK) and some stations from the Swedish National Seismic Network (SNSN) including station HFC2. With a total of 276 temporary stations and 31 permanent stations, we arrived at 14 349 *P* onsets (vertical), 4611 *SV* onsets (radial) and 5070 *SH* onsets (tangential) from a total of 1256 events with $M_w > 5.5$ at teleseismic distances (30°–99°). Instruments ranged from 1 Hz to 120 s sensors. All signals were carefully corrected for these very different instrument responses and downsampled to 20 Hz. Details of the location of the individual arrays and the amount of data each has contributed are shown in Fig. 1(b) and Table 1. The event distribution is shown in Fig. 2.

METHOD

Traveltime residuals, that is, the difference between observed and calculated traveltimes for each earthquake-station pair, reflect the deviation of the 3-D real Earth from a stratified Earth reference model (such as the IASP91 model of Kennett & Engdahl 1991) along the ray. In the case of regional tomography, we are interested in velocity variations in the upper mantle beneath the area covered by the stations. The effect of velocity structure outside the study area on the residuals is reduced by subtracting the mean of residuals from the residuals of each event. The effect of the crust is subtracted using a 'known' crustal velocity and thickness model. These steps are discussed in more detail below.

Since some of the stations used in this study are short period (∼1 Hz) and very short period (>1 Hz), the instrument response removal procedure is an important step in picking the *P* wave at about 1 Hz, and a crucial step when picking the *S* wave at around 0.1 Hz. The comparison of waveforms before and after removing instrument response shows the significant improvement in waveform similarity which is required before picking arrival times (Fig. 3).
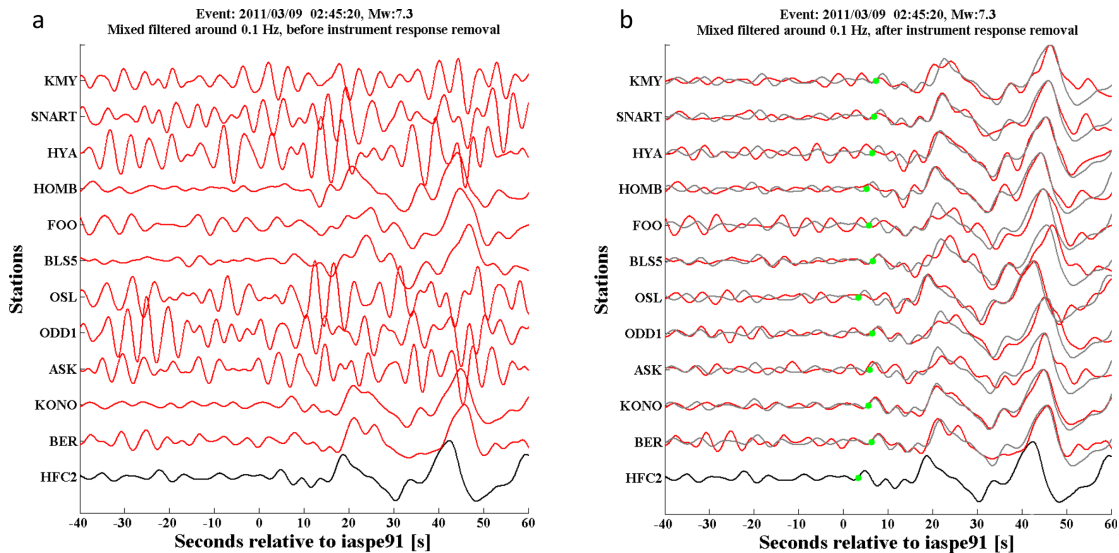
Figure 3. Example of picking process for *SH*-wave on *T* component for event 2011/03/09 02:45:20; M_w 7.3. Waveforms are filtered using mixed-phase-filter (Medhus *et al.* 2012b) at 0.05–0.2 Hz. Station HFC2 is selected as the reference station (black waveform). (a) Raw waveforms before removing the instrument response. (b) Waveforms after correction for instrument responses. Green dots and grey waveforms show shifts of reference station waveform after cross-correlation. Clearly, correction for instrument response is crucial when correlating the broad-band station HFC2 to short period stations like HYA and SNART.

The *P*- and *S*-wave arrival times were determined using an improved cross correlation technique presented in Medhus *et al.* (2012a) combined with a careful manual check. We used the mixed phase procedure described in Medhus *et al.* (2012b) to filter *P* waves around 1 Hz and *S* waves around 0.1 Hz.

Synthetic traveltimes for *P* and *S* waves were computed using the IASP91 velocity model. The importance of having a uniform event list (catalogue of origin time and hypocentre location of each event) is discussed at length in Medhus *et al.* (2012b). We used the recalculated USGS catalogue (recalculation by USGS was done in 2012).

We calculated the effect of the Earth's ellipticity on arrival times using the expressions and tabulated values in Kennett & Gudmundsson (1996). In order to minimize the effect of different thicknesses and velocity structure of the crust, the common procedure is to subtract the effect of a known crustal velocity structure from the background model (IASP91) for each ray path in the crust. We employed the same crustal velocity model as Medhus *et al.* (2012a) which inserts the high-resolution information of sedimentary thickness and velocities of the Danish and North German Basins into the crustal velocity model of Tesauro *et al.* (2008). Tests in Medhus *et al.* (2012a) showed that likely errors related to realistic uncertainty in crustal thickness and velocity in the study area are of the order of ±0.1 s.

These corrected traveltime residuals were fed into a conventional relative tomographic inversion, following the procedures described in Medhus *et al.* (2012a). We parameterized the study area using $50 \times 50 \times 50$ km^3. Further details of the inversion as well as the resolution and recovery of synthetic anomalies are given in the 'Regularization and resolution analysis' section below.
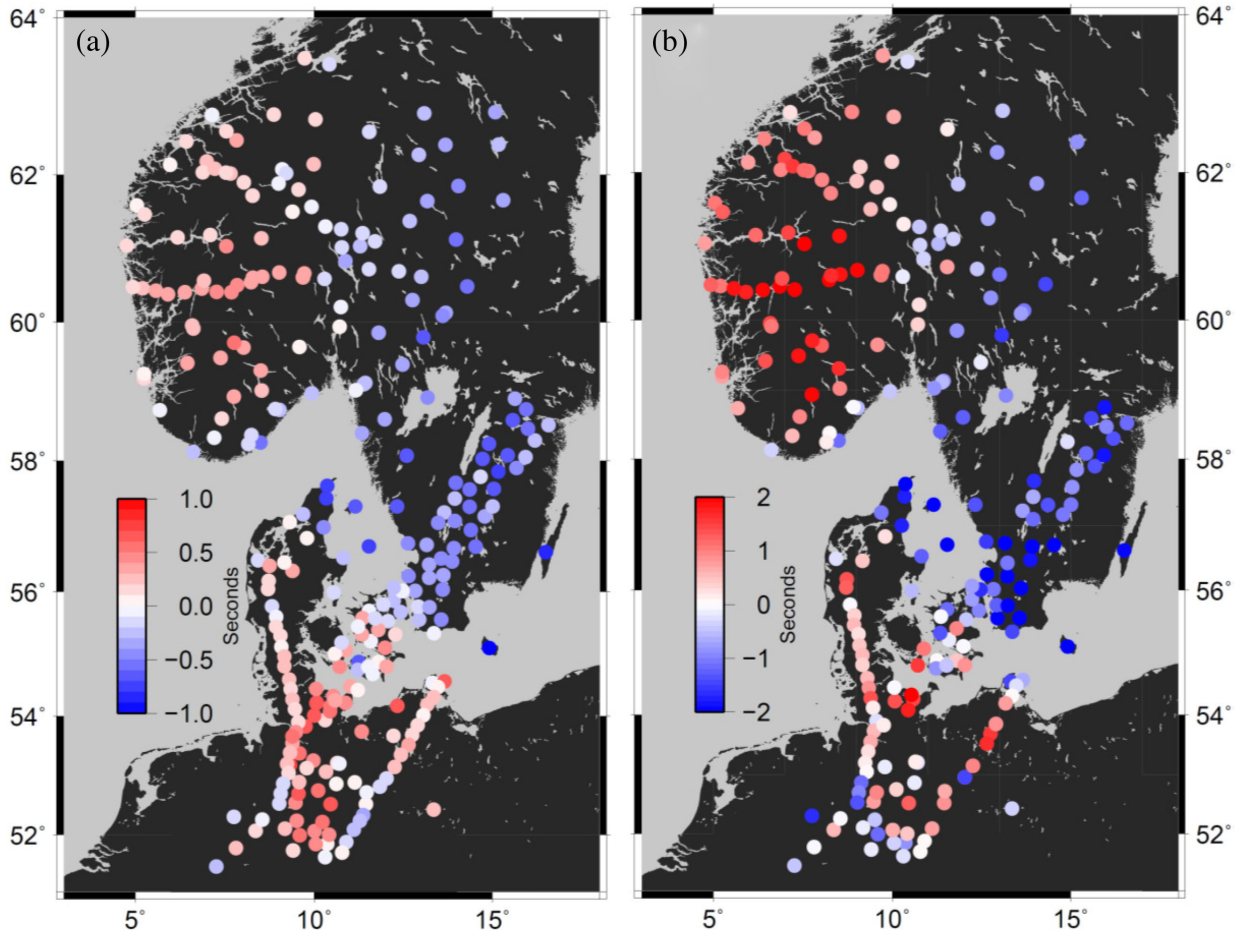
REFINEMENT OF TRAVELTIME RESIDUALS

All arrival time measurements went through a number of quality control steps in order to eliminate outliers and minimize the amount of noisy data. The first step was a visual assessment of signal-to-noise ratio, giving each event a quality level (ranging from 1 for very noisy data to 8 for high-quality data. For later calculations we used only events within the quality range of 3–8). The second quality control step involved comparison with the reference station HFC2. This station is a permanent station with generally high signal-to-noise ratio, located on bedrock in southern Sweden, where it has been recording during most of the study period (2002–2012). Traveltime residuals were excluded if they deviated more than ±5 s from the HFC2 traveltime residual. Moreover, residuals at stations showing a trend, or sudden change in time (e.g. due to wrong GPS correction for leap second), were excluded or corrected.

Finally, we sorted arrivals based on the deviation from the median of the traveltime residuals for each event and excluded arrivals deviating more than ±1.5 s for the *P* wave and ±3.0 s for the *S* wave. The application of these criteria reduced the number of *P* residuals from 14 349 to 14 079, *SV* residuals from 4611 to 4502 and *SH* residuals from 5070 to 4962, indicating that the vast majority of residuals are within ±1.5 s of the median residual for *P* waves and ±3.0 s of the median for *S*-waves for each event.

After these quality-enhancing steps the traveltime residuals were assessed in two ways. First, we produced maps of regional station residuals in the following way. The station HFC2 has been used as a reference station because it has permanent recording at a high signal-to-noise ratio, and it is located on bedrock outside the more complicated setting of the Oslo Graben. As the first step, the residual measured at HFC2 for a given event was subtracted from all other station residuals measured for the same event. At each station we then computed the mean of all these residuals relative to the common reference, HFC2. Somewhat arbitrarily, HFC2 therefore came out with a station mean residual of zero. Finally, we subtracted the mean of all these station mean residuals. The resulting equalized station mean residuals, which are visualized in Fig. 4, will therefore have a sum which is zero and a spread generally within ±1 s for *P*-wave residuals and, as expected, larger, up to about ±2 s for *S*-wave residuals. We note that the previously identified pattern in *P*-wave residuals, with early arrivals to the east (Swedish shield area) and late arrivals in the Danish and North German Basins to

Figure 4. Mean relative traveltime residual at each station for (a) *P* wave and (b) for *S* wave (including both radial and tangential components). Reference zero is defined as the mean of all individual station mean values. A general pattern of early arrivals to the east and later arrivals to the west is clearly seen, with the strongest contrasts in the *S* residuals.

southwest of the Tornquist Zone (Medhus *et al.* 2012a), is even more strongly imaged by the *S*-wave residuals. Second, the residuals were subjected to inversions, leading to tomograms of relative anomalies in *P*-wave velocity, *S*-wave velocity and the V_P/V_S ratio, as described below.

INVERSION RESULTS

P- and *S*-wave tomography

The *P*- and *S*-velocity tomography models are presented in Figs 5 and 6, respectively. Cells with ray coverage below a threshold (here 200 km cumulative ray length per cell) have been blanked. The *P*-velocity tomography model confirms and extends the general pattern revealed in previous works (Medhus *et al.* 2012a), with a prominent upper-mantle velocity boundary (UMVB) separating generally low mantle *P* velocity in the Danish Basin, most of the North German Basins and in southern Norway, and generally high *P* velocity in shield areas of southern Sweden.

In general, our *S*-velocity model shows a pattern very similar to the *P*-velocity model, but generally with even stronger contrasts (Fig. 6). In particular, the same regional upper-mantle boundary is recovered. There are differences, however, such as the kink in the Kattegat Sea where the regional boundary swings northwards away from the STZ. Here we see a distinct sharp boundary in *S*-velocity,

whereas the *P* velocity shows a more diffuse low contrast boundary. These differences already point towards anomalies in the V_P/V_S ratio.
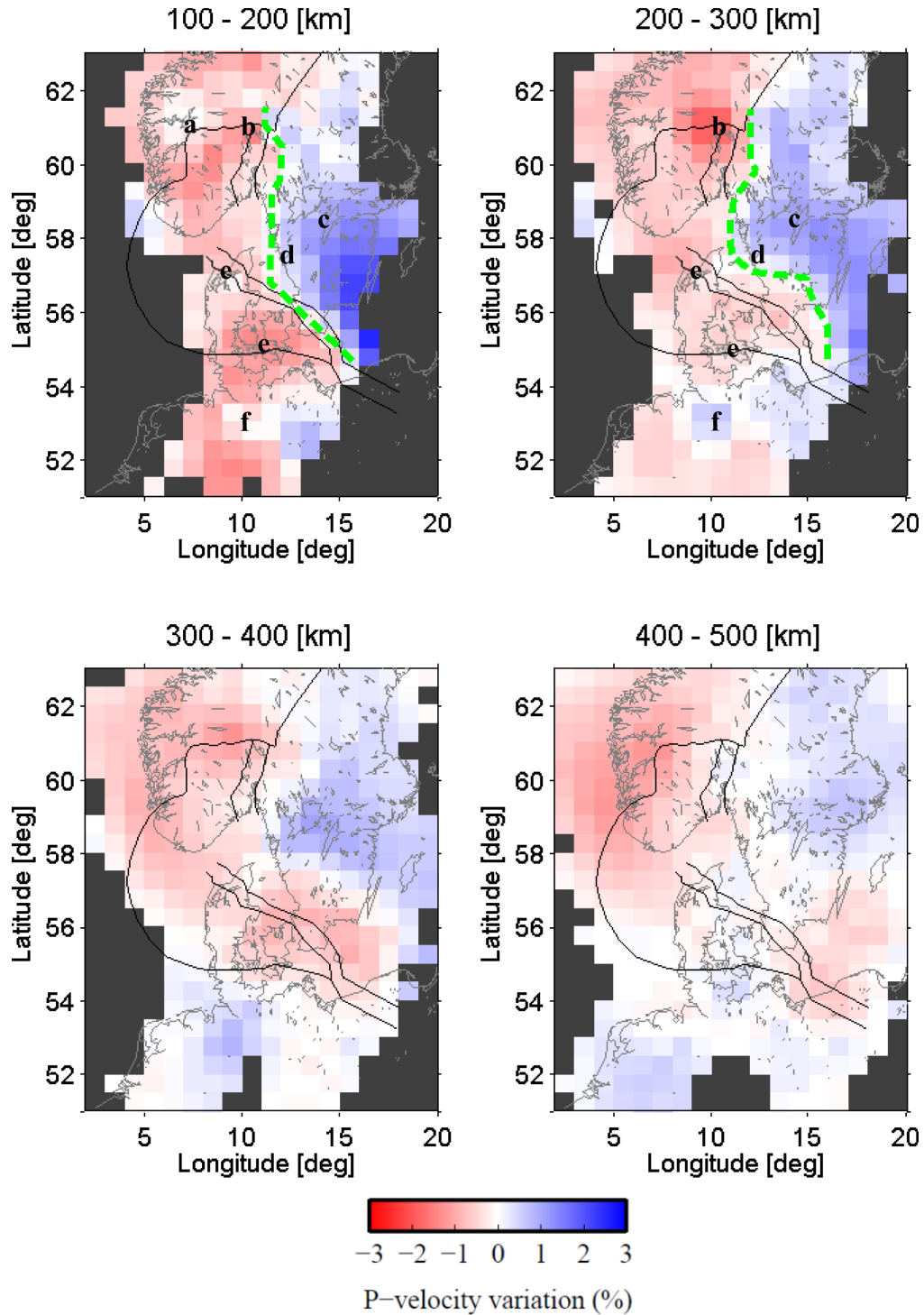
V_P/V_S variations

Fig. 7 shows the implied contrasts in the V_P/V_S ratio. We have derived the relative anomalies in V_P/V_S from the relative anomalies in V_P and V_S through the following simple approximations. All anomalies are computed in principle relative to the IASP91 model. Thus

$$\frac{\Delta\left(V_P/V_S\right)}{V_{P,IASP}/V_{S,IASP}} = \frac{V_P/V_S - V_{P,IASP}/V_{S,IASP}}{V_{P,IASP}/V_{S,IASP}} \tag{1}$$

By dividing the denominator into the terms in the numerator we get

$$\frac{\Delta\left(V_P/V_S\right)}{V_{P,IASP}/V_{S,IASP}} = \frac{V_P}{V_{P,IASP}}\frac{V_{S,IASP}}{V_S} - 1$$

$$= \left(\frac{(V_P - V_{P,IASP})}{V_{P,IASP}} + 1\right)$$

$$\times \left(\frac{(V_S - V_{S,IASP})}{V_{S,IASP}} + 1\right)^{-1} - 1 \tag{2}$$

Figure 5. Modelled *P*-wave velocity variations in four depth intervals as indicated. (Model depth interval is 50 km. Each figure thus represents an average of two layers.) Black lines show main tectonic boundaries (STZ, CDF and OG, *cf*. Fig. 1a). The green dashed line shows the position of the main Upper Mantle Velocity Boundary (UMVB) as determined from this *P*-wave model. Letters indicate prominent anomaly features discussed in the text *cf*. Table 2.

If we assume that $\frac{\Delta V}{V} \ll 1$, with $\Delta V \equiv V - V_{IASP}$ for both *P* and *S* velocities (using simple approximation for small $x, \frac{1}{1+x} \cong 1 - x$ and $x^2 \approx 0$), we may simplify the expression for the relative anomalies

$$\frac{\Delta \left(V_P/V_S \right)}{V_{P,IASP}/V_{S,IASP}} = \frac{(V_P - V_{P,IASP})}{V_{P,IASP}} - \frac{(V_S - V_{S,IASP})}{V_{S,IASP}} \quad (3)$$

This means that the relative anomaly in V_P/V_S is equal to the relative anomaly in V_P minus the relative anomaly in V_S. Change in V_P/V_S is believed to be an important indication of change in composition of upper-mantle rocks (see below).

Our V_P/V_S model shows a distinct contrast of ± 1–2 per cent across the main UMVB. This prominent feature is very stable down to a depth of 200–300 km, indicating the existence of significant upper-mantle compositional differences, in addition to thermal
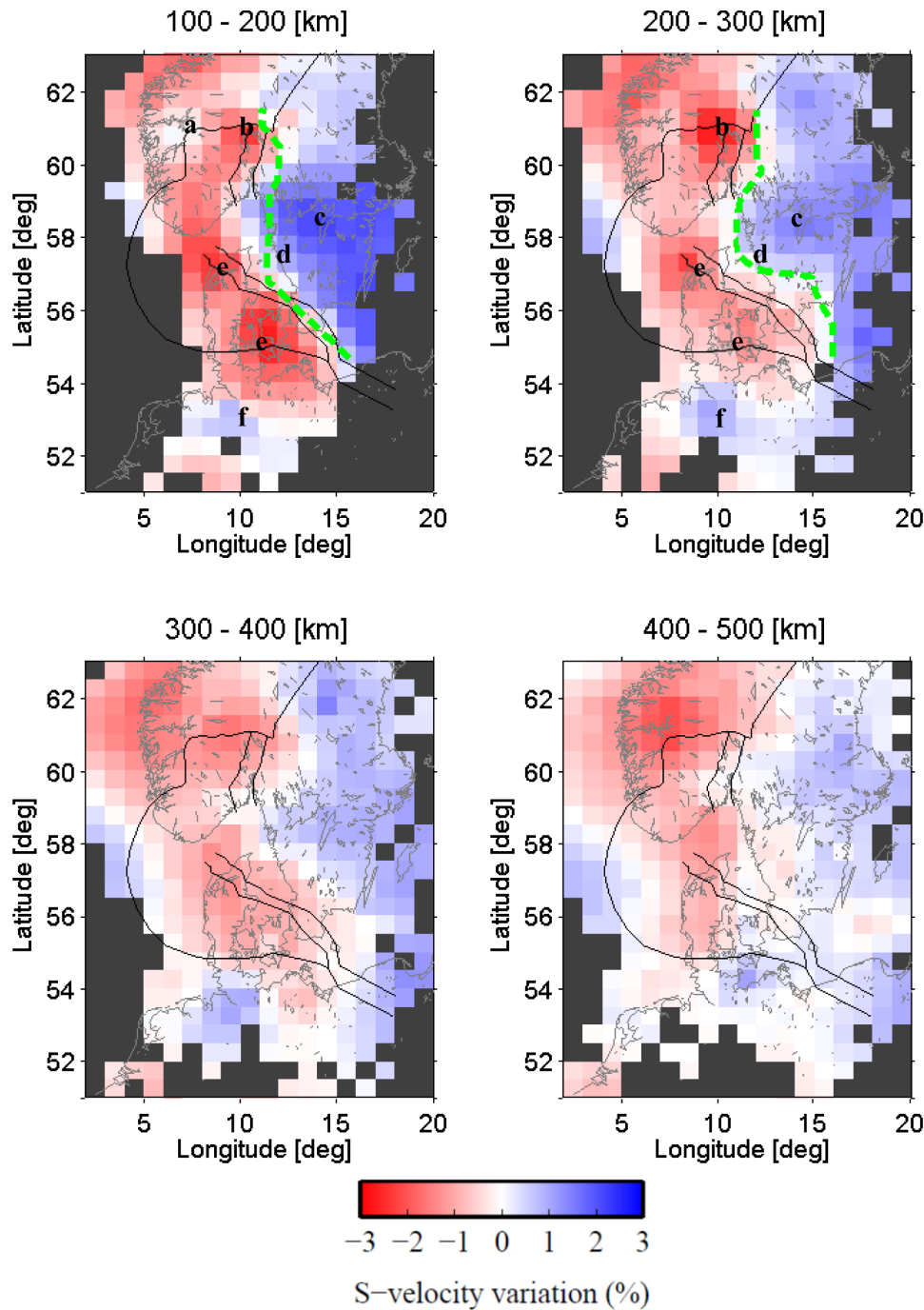
Figure 6. Modelled *S*-wave velocity variations. Figure outline as in Fig. 5. As a reference, the position of the green dashed line is that determined by the *P*-wave model (Fig. 5).

differences, in this region. Fig. 8 highlights three vertical sections, AA′, BB′ and CC′, which cross the main structural units and areas of main velocity variations (for location see Fig. 1a).

Regularization and resolution analysis

The inverse equation for modelling seismic velocity variations may be summarized as

$$\mathbf{m}_{est} = \left(\mathbf{A}^T \mathbf{A} + \frac{\sigma_{obs}^2}{\sigma_0^2} \mathbf{I} + \frac{\sigma_{obs}^2}{\sigma_{xy}^2} \mathbf{G}^T \mathbf{G} \right)^{-1} \mathbf{A}^T \mathbf{d}_{obs}$$

where $\mathbf{m}_{est}$ is the vector of slowness anomalies (inverse of the velocity); the matrix $\mathbf{A}$ contains ray lengths in cells; σ_{obs} is the observation error standard deviation; σ_0 is the assumed standard deviation of the slowness anomalies; σ_{xy} is the assumed standard deviation of the difference between cell slowness and mean slowness of neighbour cells in the same plane; $\mathbf{G}$ is the matrix describing the constraint of slowness to neighbours, that is the smoothing; and $\mathbf{d}_{obs}$ is the vector of traveltime residuals. The values of the three involved standard deviations control the regularization of the slowness estimates and hence the noise rejection and the smoothing in the inverse model.
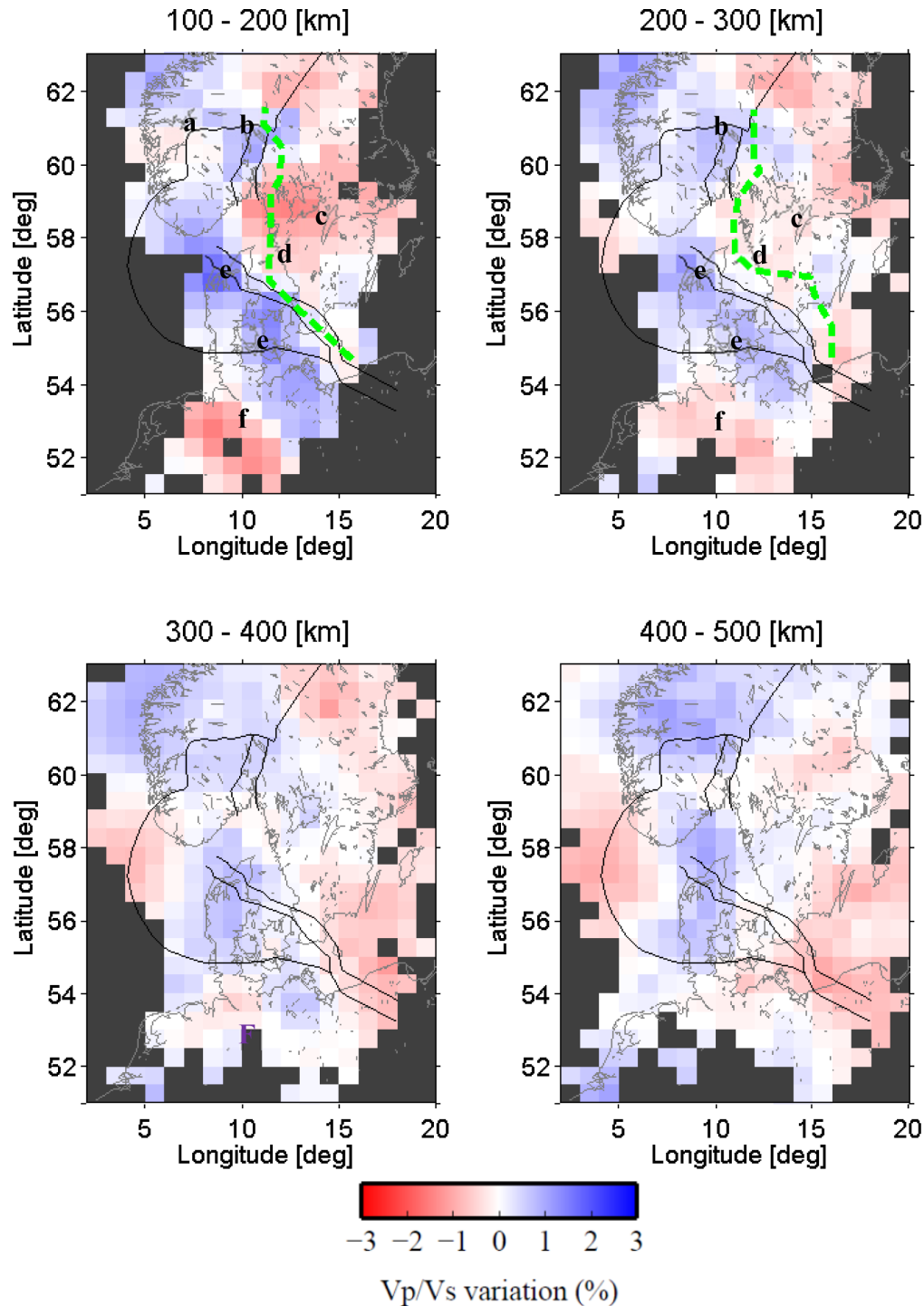
Figure 7. V_P/V_S variations calculated from the relative *P*- and *S*-wave velocity variations in Figs 5 and 6, respectively. Figure outline as in Fig. 5, including the dashed green line.

Based on previous experience, we regard slowness deviations of 3 per cent as likely, so we used $\sigma_{P0} = 0.03 \times (V_{P\text{-IASP}})^{-1}$. For the *P*-velocity inversion, a subjective assessment of arrival time uncertainty led us to the value $\sigma_{Pobs} = 0.2$ s. A conventional L-curve study led to a choice of $\sigma_{Pxy} = 0.0025 \times (V_{P\text{-IASP}})^{-1}$. The resulting *P*-velocity model in Fig. 5 defines model data which fit the observed data with an RMS misfit of 0.18 s. This is nicely consistent with the observational error assumed above. The total variance of the observed data is 0.11 s² compared with a misfit

variance of $(0.18 \text{ s})^2 = 0.032 \text{ s}^2$. The variance reduction factor is therefore 0.30.

For the *S*-velocity inversion, the traveltime residuals may be expected to be about $\sqrt{3}$ times higher, measured in seconds, if a typical V_P/V_S ratio of $\sqrt{3}$ is assumed. The observational error is also expected to be somewhat higher because arrival times are read at much lower frequencies. However, in order to avoid a bias in V_P/V_S owing to different regularization of the *P*-velocity models and the *S*-velocity models, it is mandatory that both inversions
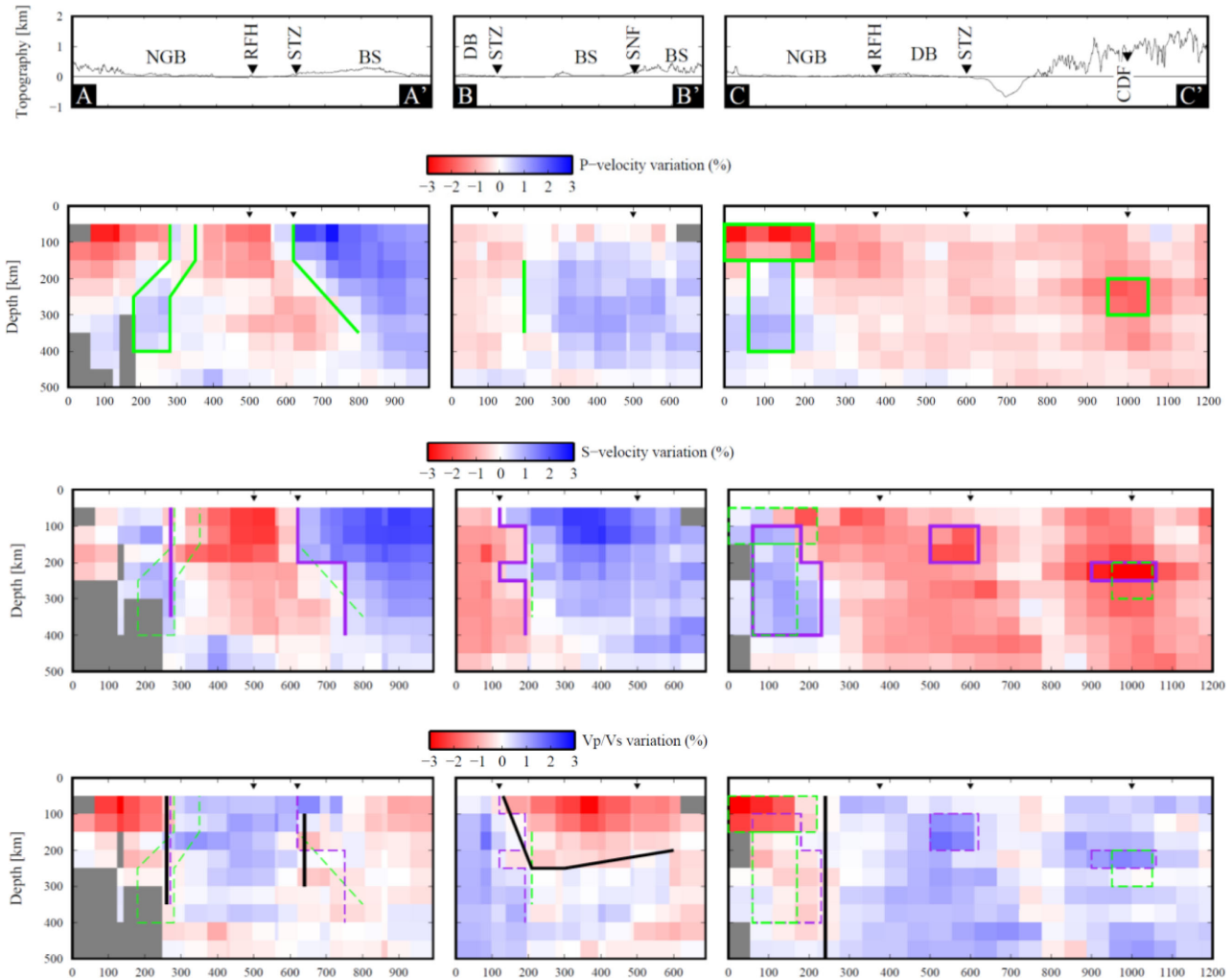
Figure 8. *P*-wave velocity, *S*-wave velocity and V_P/V_S ratio variations (upper, middle and lower panels, respectively) along three cross sections, AA′, BB′ and CC′ (locations in Fig. 1a). Topography (vertical exaggeration) and main tectonic and geological elements are indicated in the top panel (BS, Baltic Shield; CDF, Caledonian Deformation Front; DB, Danish Basin; NGB, North German Basin; RFH, Ringkøbing Fyn High; SNF, Sveconorwegian Front; STZ, Sorgenfrei-Tornquist Zone). Major anomaly features with high contrast are outlined with green in the *P* model, with purple in the *S* model and with a black line in the V_P/V_S model.

have the same degree of regularization. This is achieved by selecting $\sigma_{S0} = 0.03 \times (V_{S\text{-IASP}})^{-1}$, $\sigma_{Sxy} = 0.0025 \times (V_{S\text{-IASP}})^{-1}$ and $\sigma_{Sobs} = 0.2 \text{ s} \times V_{P\text{-IASP}}/V_{S\text{-IASP}} \cong 0.35 \text{ s}$.

The resulting *S*-velocity model in Fig. 6 defines model data which fit the observed data with an RMS misfit of 0.65 s. This is clearly larger than the above assumed observational error. Similarly, at a fixed V_P/V_S ratio we would expect the *S* residuals to be larger than the *P* residuals by a factor of about $\sqrt{3}$, implying a data variance of $0.11 \text{ s}^2 \times 3 = 0.33 \text{ s}^2$. The actual total variance of the observed *S* data is 1.16 s^2, that is, higher by a factor of more than 3. This reflects the marked anomalies in V_P/V_S ratio which emerge in Fig. 7. The theoretical *S*-wave residuals of the *S*-velocity model in Fig. 6 have a misfit variance of $(0.65 \text{ s})^2 = 0.42 \text{ s}^2$. Thus, for the *S*-velocity inversion the variance reduction factor is 0.37.

We analyse resolution in two ways. First, we perform a classical checkerboard test with blocks of a size comparable to the units we see in the tomograms (Figs 5 and 7). Second, we define a simple synthetic structural model which in more detail mimics the main structural features that were identified in the real-data tomograms. We take great care to use exactly the same ray coverage and regularization in these synthetic tests as for production of the real

tomograms. Hence, the degree of recovery of checkerboard patterns, as well as the features of the specific structural model, serves as validation of the interpretations we may draw from the real-data tomograms.

V_P and V_S resolution

Fig. 9 shows the input checkerboard for both *P* and *S* models. It consists of 150 × 150 km alternating blocks (with ±4 per cent velocity contrast) separated by 50 km neutral zones. Blocks occupy the depth intervals 100–200, 250–350 and 400–500 km, thus leaving 50 km thick blank intervals. Figs 10 and 11 show the recovery of this checkerboard in *P* and *S* models, respectively.

For the *P* tomography (Fig. 10), we observe a recovery of clear block outlines, however with significant upward smearing to the interval just below the crust (50–100 km). At deeper levels (greater than 250 km), the block contours are still nicely resolved, but the amplitudes are below 50 per cent of the 'real' velocity contrasts in the synthetic model. This indicates that lateral resolution of boundaries may be reliable even down to the greatest depths, but real
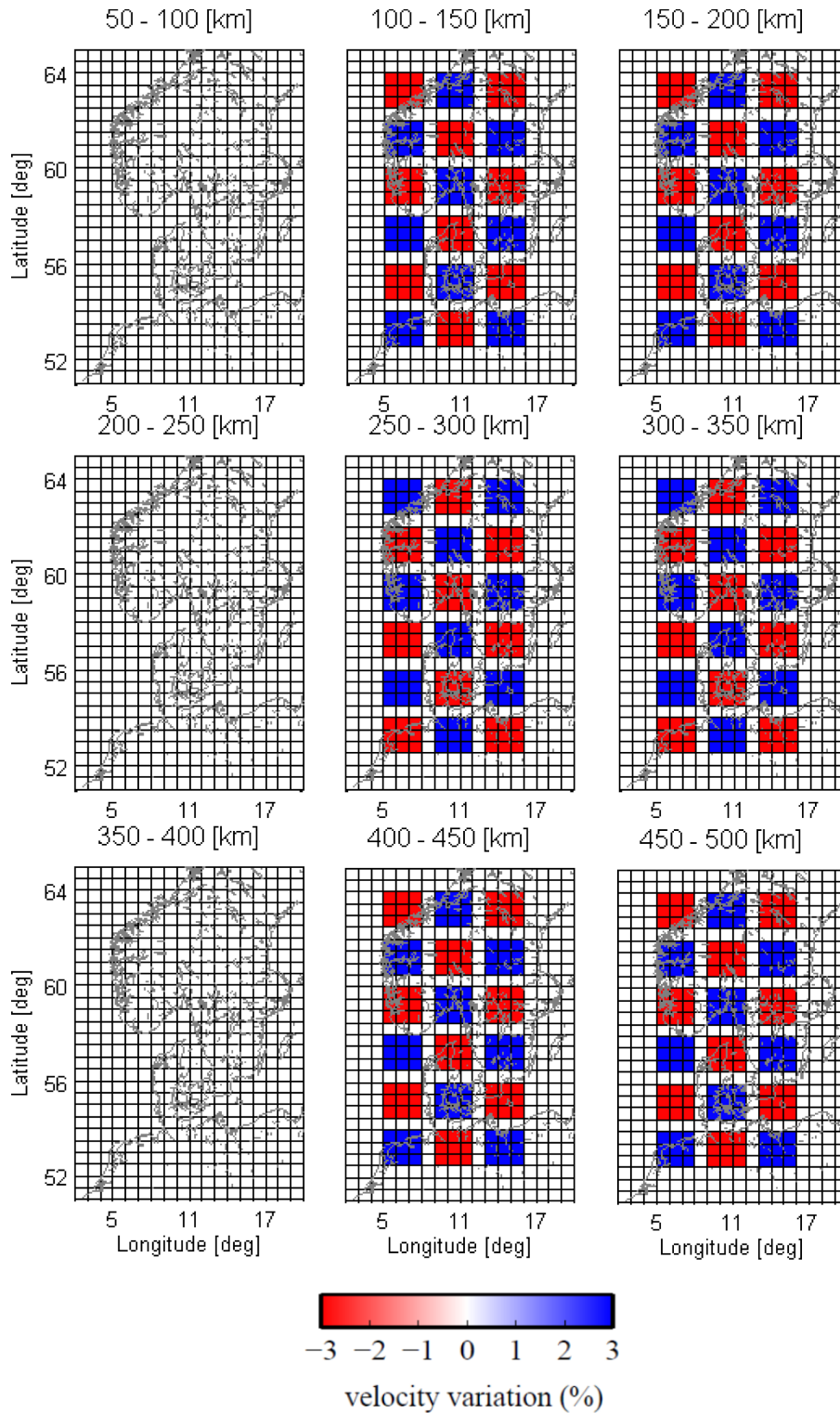
Figure 9. The input checkerboard model, ±3 per cent, tested for both *P* and *S* waves.

velocity variations at this wavelength are likely to be significantly larger than the modelled amplitudes. *S* velocity shows the same upward smearing to the depth interval of 50–100 km. The ray coverage is weaker (c. 5000 rays versus c. 14 000 rays in the *P* model). However, the checkerboard resolution comes out almost as well for the *S* rays as for the *P*-ray distribution, in particular in the upper depth levels. At greater depths (more than 250 km), in addition to

lower amplitude, about 50 per cent of the 'real' velocity contrast, the block contours are less clear than those of the *P* model.

Fig. 12 shows the more elaborate characteristic structural input model, which we define by inspiration from the real-data tomogram in Figs 5 and 6. This characteristic model features a boundary between thick and thin lithosphere. The blocks cover depths of 100–300 km with velocity differences of up to ±3 per cent. In the
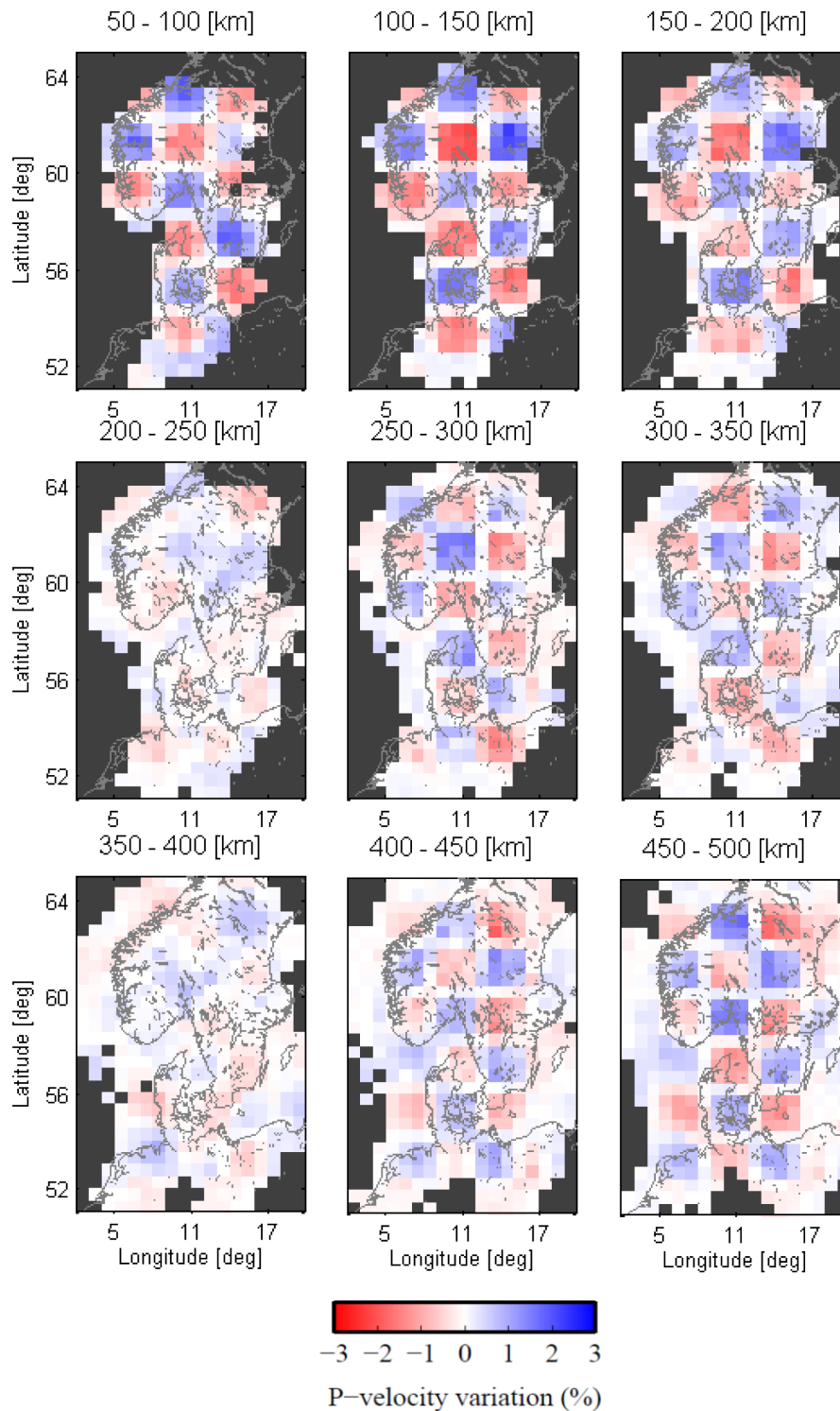
Figure 10. Results of checkerboard test for *P* wave.

North German Basin we include a deep high-velocity block at the depth interval of 200–300 km.

The result of forward computation of synthetic anomalies, followed by inverse tomography, is shown in Figs 13 and 14 for *P* and *S* waves, respectively. We see considerable vertical smearing. Thus, both low- and high-velocity features smear upwards to the mantle just below the crust (50–100 km), as well as downwards to below 300 km. However, still we observe good recovery of amplitudes and lateral boundaries are very well recovered in this synthetic test in both *P* and *S* models, and the downward-smearing is only moderate.

V_P/V_S uncertainty estimation

The V_P/V_S ratio variation, calculated directly from V_P and V_S variations, may easily be affected by different resolution and different
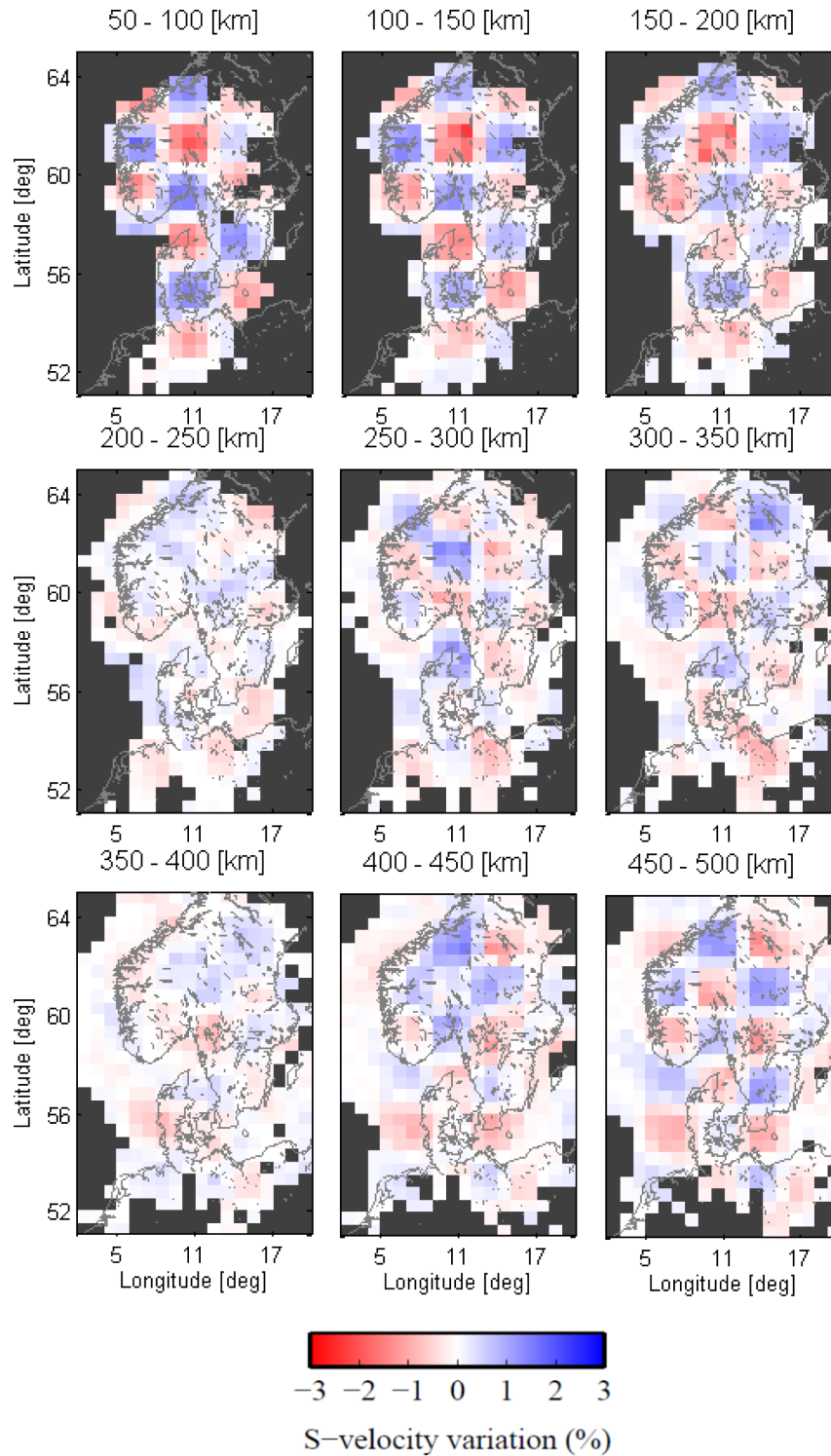
Figure 11. Results of checkerboard test for *S* wave.

ray coverage in *P* and *S*. Fig. 15 shows the recovery of V_P/V_S in the characteristic model. The V_P/V_S ratio in this characteristic model is constant, so the relative model anomalies in V_P/V_S are zero. Indeed, Fig. 15 shows a very faint pattern which represents the noise level owing to actual differences in ray coverage in *P* and *S* and the associated different influence of regularizations. The inversion of the real data reveals significantly larger V_P/V_S ratio variations, of

up to ± 2–3 per cent, that is, comparable to the recovered *P*-model contrasts.

DISCUSSION AND CONCLUSIONS

Based on careful analysis of about 20 000 waveforms collected in several separate projects over a period of about 15 yr in southern
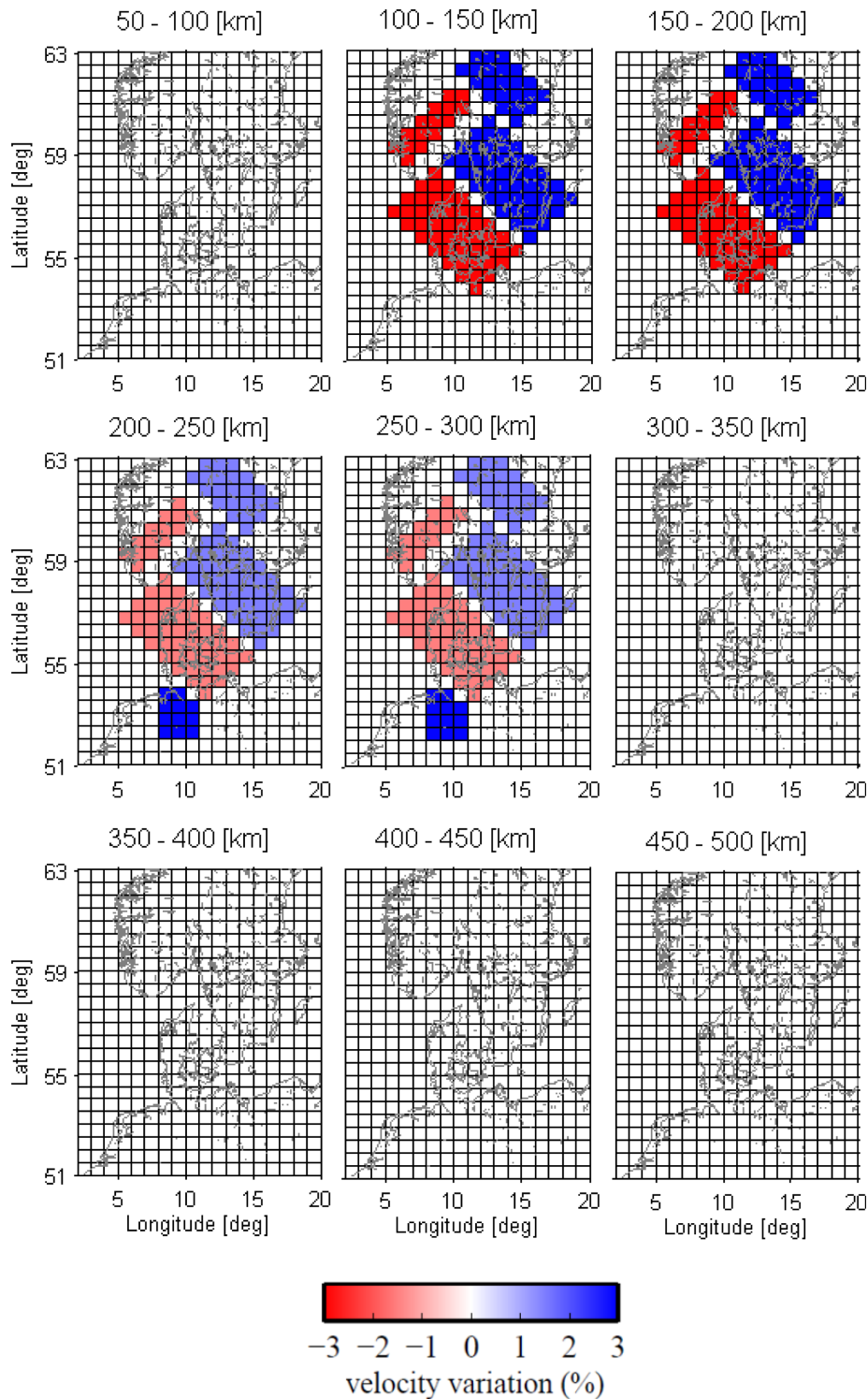
Figure 12. Synthetic characteristic structural input model. This test resembles a plausible scenario with thick homogenous lithosphere beneath the Baltic Shield in southern Sweden and shallow, low-velocity asthenosphere (thin lithosphere) beneath the Danish Basin. In the North German Basin, the resolution of a local high-velocity body (depth interval of 200–300 km) is tested. Southern Norway includes a zone of low velocity and boundaries to high velocities.

Scandinavia and northern Germany, we have defined tomograms of relative anomalies in *P*-wave velocity, *S*-wave velocity and V_P/V_S ratio. Resolution analysis has been performed in terms of both checkerboard tests and characteristic structure models, inspired by the real-data tomograms. Some vertical smearing is observed, as would be expected, given the generally near-vertical ray direction

inherent in regional teleseismic traveltime tomography. Still, the lateral resolution is very good, as would also be expected.

The *S*-wave traveltimes are defined from signals with a dominant frequency of about 0.1 Hz, so significant sensitivity away from the geometric ray path is expected; at a depth of 300 km the radius of the first Fresnel zone is about 75 km. Note, however, that the
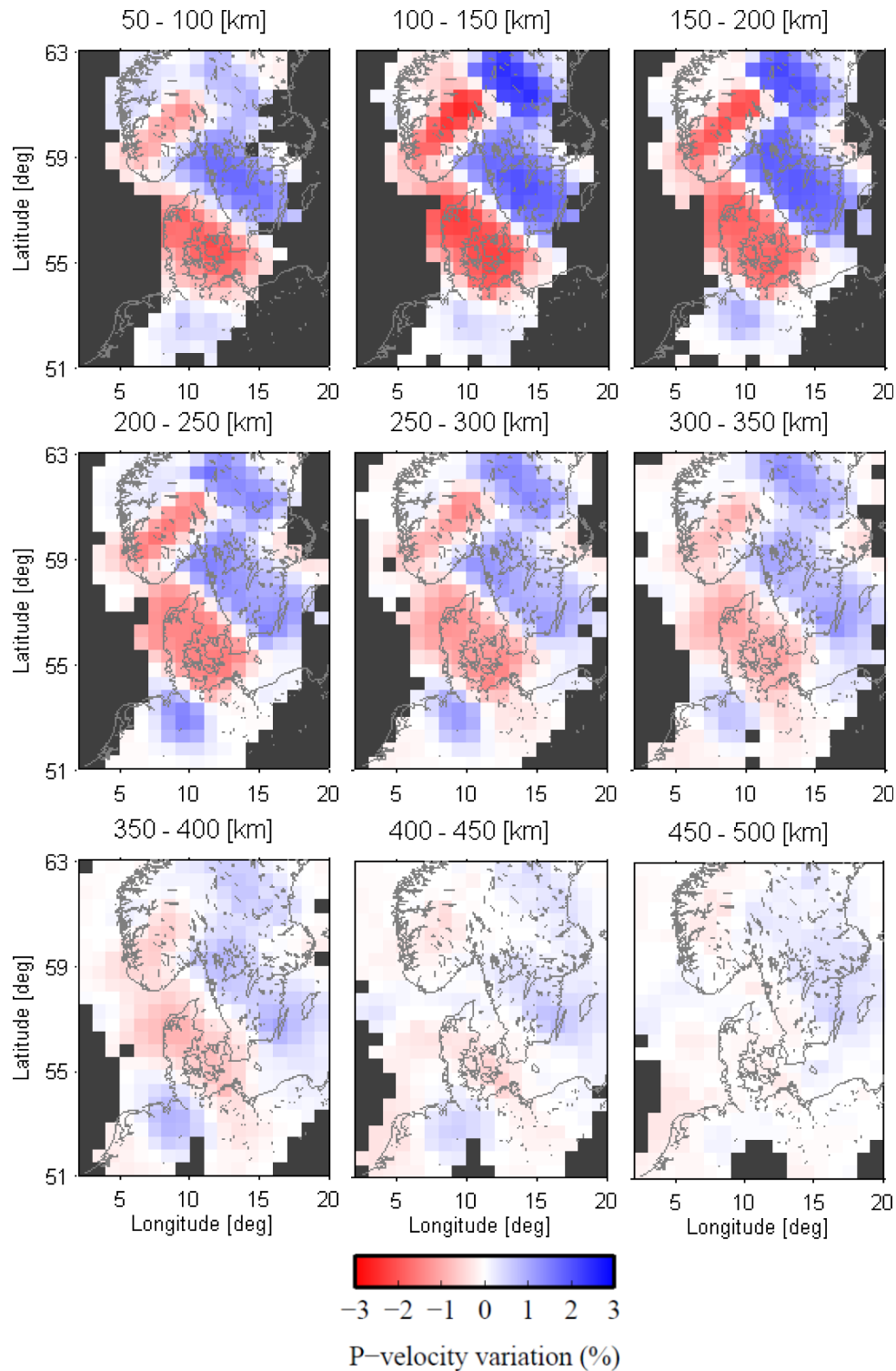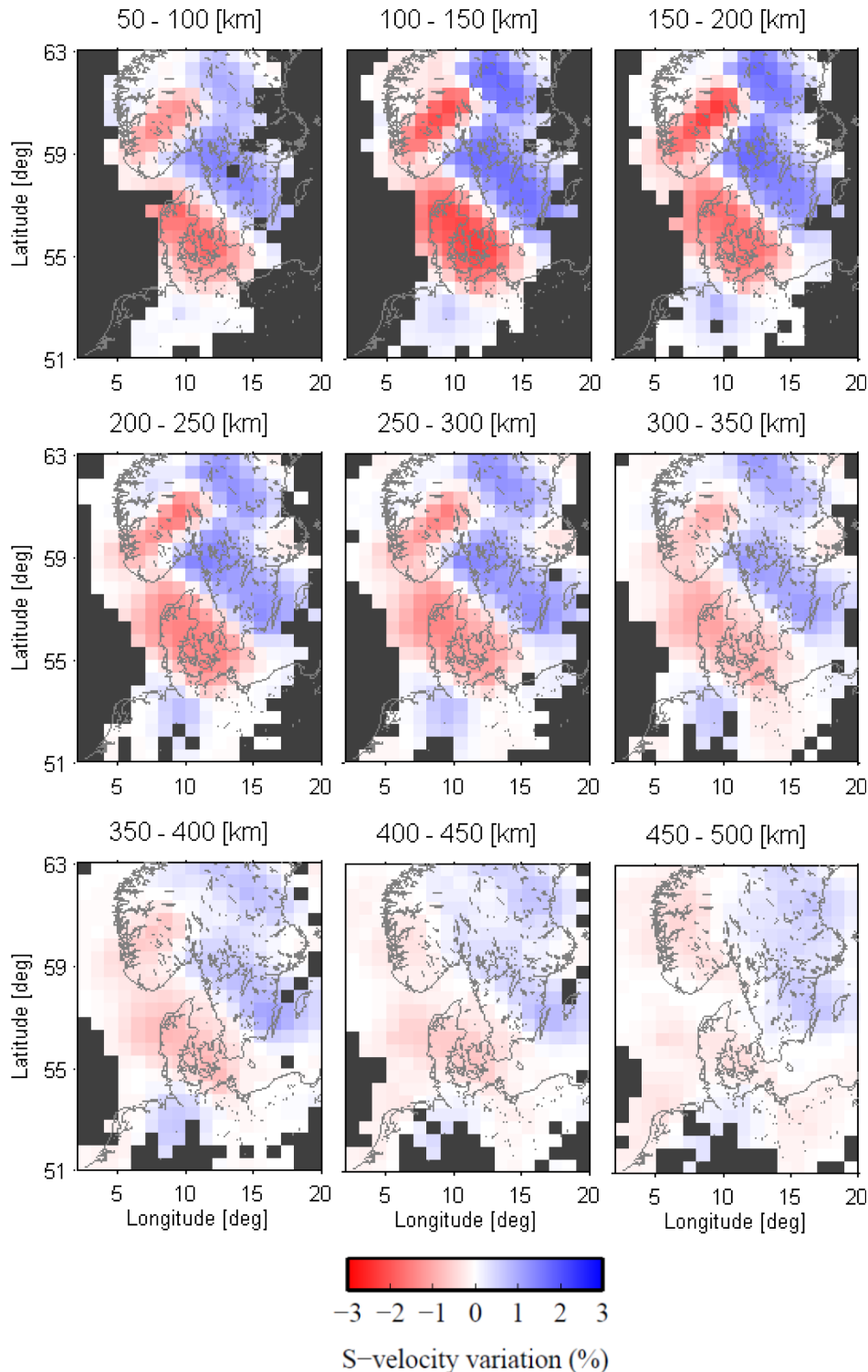
Figure 13. Recovery of *P*-wave model for the structural test presented in Fig. 12.

characteristic model analysed is composed of larger blocks, so the resolution of these larger structures is not likely to be invalidated by finite-frequency effects. We may therefore proceed to the interpretation of velocity variations and anomalies exposed as horizontal section in Figs 5 to 7 and as three vertical sections in Fig. 8.

Main velocity anomalies, 100–300 km depth

The main UMVB is clearly outlined at depths of 100–300 km in both the *P*-wave and the *S*-wave models (Figs 5, 6 and 8). It follows the boundary found in Medhus *et al.* (2012a) based on *P* tomography alone. The UMVB defines a generally very narrow velocity

Figure 14. Recovery of *S*-wave model for the structural test presented in Fig. 12.

transition that rather closely follows the trace of the STZ in most of the Danish area, but continues north into southern Norway.

In the following we focus mainly on the *S*-velocity structure and the V_P/V_S ratio contrasts implied by the *P* and *S* tomograms. The main *S*-velocity transition closely follows the transition found in the *P* velocity. In the southernmost part the transition at the level 200–300 km is displaced towards northeast, relative to that of depth 100–200 km, implying a dip of about 45° in this direction

(consistent with the results of Voss *et al.* 2006). Near (12°E, 57.5°N, termed the 'Kattegat Bend') the boundary bends northwards with a particularly high *S*-velocity zone centred at 14°E, 58.5°N (termed the 'South Sweden Fast Zone' and marked c in Figs 5 and 6). At this location the boundary is near-vertical. The main boundary runs just east of the Oslo Graben.

The UMVB separates two main anomaly features, the 'South Sweden Fast Zone' and a prominent low-velocity region, termed the
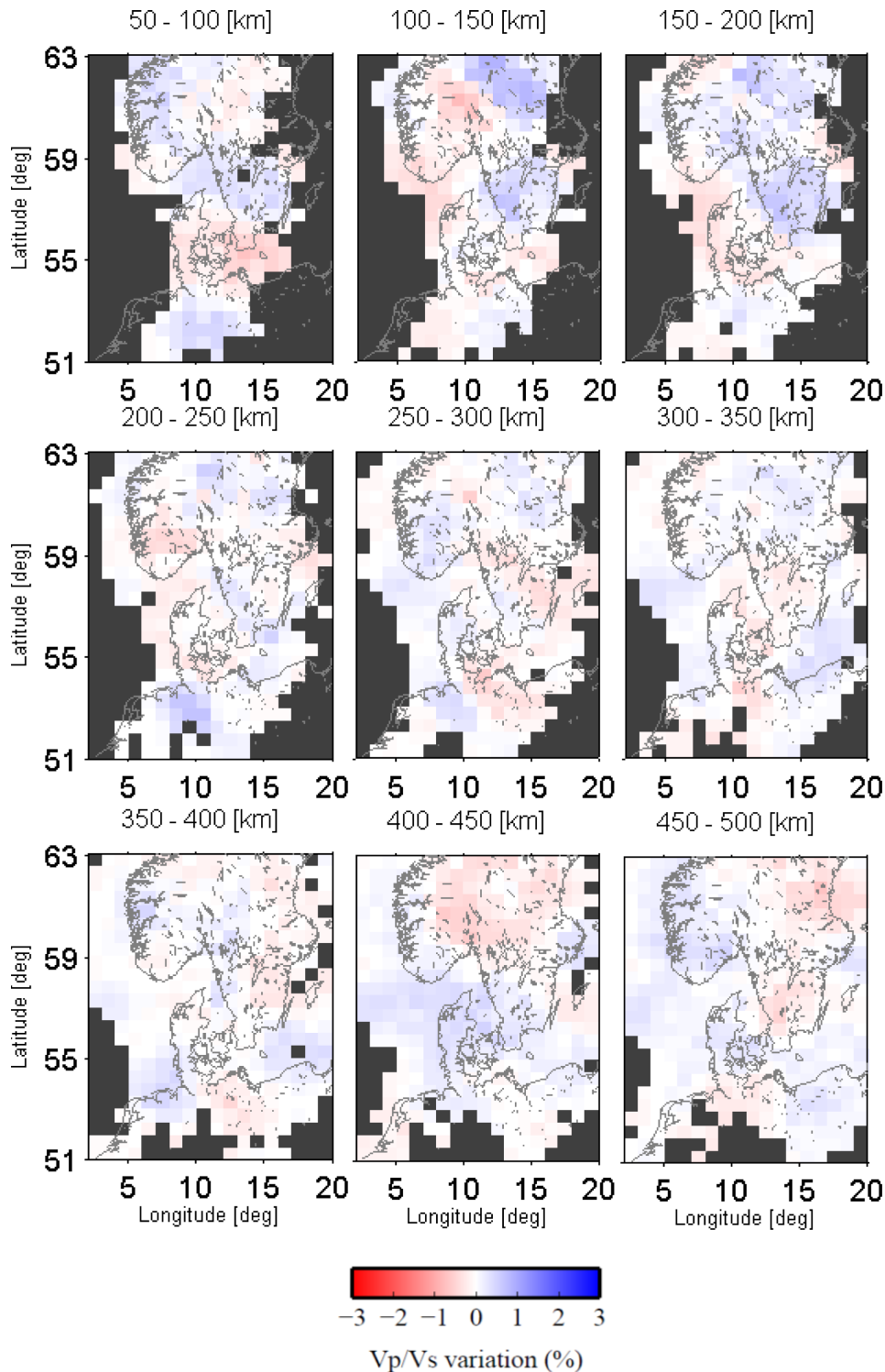
Figure 15. Recovery of V_P/V_S ratio for the structural test model presented in Fig. 12. Because identical relative contrasts are used in V_P and V_S, expected values are zero for all cells. The low level of the recovered ratio quantifies the inversion noise level owing to differences in ray coverage for S and P waves.

'Danish Slow Zone' (marked e in Figs 5 and 6), which is aligned from around (9°E, 57°N) to around (11°E, 55°N), running from the Skagerrak through most of the Danish area and extending south into the northernmost part of Germany. This 'Slow Zone' is apparent in both P and S models and in particular as a pronounced S-anomaly (down to −2 to −3 per cent) in the 100–250 km depth interval (Figs 6 and 8).

A particularly deep local minimum in S-velocity, as well as in P velocity, is found northwest of the Oslo Graben around (10°E, 61°N), called the 'South East Norway Slow Spot' and marked b in Figs 5 and 6. In western Norway (near Sognefjord and Hardanger Fjord), relatively higher S-velocities are found at 100–200 km depth (7°E, 61°N), termed the 'Southwest Norway Fast Spot' and labelled a in Figs 5 and 6. At the southernmost end of the resolved model

Table 2. Summary of characteristics of main velocity anomaly features with approximate anomaly centres (*cf.* Figs 5, 6 and 7).

	Longitude	Latitude	Main depth (km)	δV_P (per cent)	δV_S (per cent)	$\delta V_P/V_S$ (per cent)
Main upper-mantle velocity boundary (UMVB)	15°E to 12°E	54°N to 62°N	100–300	±1	±1–2	±1–2
Southwest Norway Fast Spot, labelled a	7°E	61°N	100–200	∼0	∼0	∼0
Southeast Norway Slow Spot, labelled b	10°E	61°N	100–300	−2	−3	+1
South Sweden Fast Zone, labelled c	14°E	58.5°N	100–300	+1	+2	−1
Kattegat Bend, labelled d	12°E	57.5°N	100–300	±1	±2	±1
Danish Slow Zone, labelled e	9°E to 11°E	57°N to 55°N	100–250	−1	−2 to −3	+1 to +2
North German Fast Spot, labelled f	10°E	53°N	100–300	+0.5	+1	−0.5

volume (10°E, 53°N, f in Figs 5 and 6), we see an enigmatic deep fast region, termed the 'North German Fast Spot'. This high-velocity mantle body was also resolved by the Tor project in several studies (*cf.* Gregersen *et al.* 2002, 2010). As the Tor picks are included in the present study, we have validated this high-velocity anomaly by performing an inversion using only the new JULS data, where station locations differ from station locations in the Tor project (*cf.* Fig. 1b). This inversion was based on the ray-adapted tomography procedure described in Hejrani *et al.* (2014). The resulting velocity anomalies discussed above are summarized in Table 2.

The fact that *S*-velocities generally show stronger contrasts than *P* velocities implies that there will be contrasts in the V_P/V_S ratio aligning with the velocity anomalies. In general, this is indeed the case (Fig. 7). Note that where V_P is relatively high and V_S is relatively even higher (both blue colour) the V_P/V_S ratio will be relatively low and hence show up as red. Similarly, relative high V_P/V_S ratios (blue) are seen in areas of relatively low V_P and even lower V_S. We observe that high V_P/V_S ratios dominate southwest of the UMVB, whereas relatively low V_P/V_S ratios dominate northeast of the boundary. The slow spot near the Oslo Graben, (b), has a relatively high V_P/V_S ratio, whereas the relative fast spots in western Norway (a), southern Sweden (c) and northern Germany (f), all have relatively low V_P/V_S ratios.

We should expect some downward smearing of the strong velocity structure at shallower depths (<300 km). We indeed observe the same main anomalies in a weakened form at depths of 300–500 km. Although the resolution tests indicated that we have some deep resolution, we hesitate to interpret the structure at these deep levels.

A very recent study by Kolstrup *et al.* (2015) performed relative tomography using an interesting combination of finite frequency sensitivity kernels and wavelet-based tomographic inversion. Their analysis is essentially based on a subset of the stations used in our paper, thus covering southern Norway, northernmost Denmark and southeastern Sweden. Their models within this area show a highly reassuring correspondence to our tomograms of V_P, V_S and V_P/V_S, thereby lending further support to the interpretations that we present below.

Temperature, composition and seismic velocities

For easy reference, although the relationships between temperature, composition and seismic velocities may be rather complex (*cf.* Artemieva 2009, 2011), we summarize some main elements that will be employed in discussion of the implications of velocity anomalies. Generally, the effects are different below the solidus, like inside the lithosphere, and close to and above the solidus, like in the asthenosphere.

In the colder part of lithosphere a temperature increase of 100 °C will decrease both V_P and V_S by about 0.7 per cent (Lee 2003) and the V_P/V_S ratio is relatively insensitive to temperature. Around the LAB (Lithosphere-Asthenosphere Boundary) and below, the *S*

velocity becomes more sensitive to temperature, typically up to 1–2 per cent per 100 °C, partly due to anelasticity effect (Cammerano *et al.* 2003), thus making also the V_P/V_S ratio temperature-sensitive at these greater depths and temperatures. Moreover, any melt will reduce mainly V_S and less so V_P, so accordingly V_P/V_S is increased by the presence of melt. Fluids will tend to decrease velocities both inside the lithosphere and below, and fluids have the added effect of decreasing the solidus temperature.

A higher degree of iron depletion, and depletion in other 'basaltic components', as reflected in the magnesium number, Mg# (100 × (Mg/(Mg + Fe)), implies higher V_S whereas V_P is largely unaffected (Lee 2003; Schutt & Lesher 2010). Up to about 1 per cent of increase in V_S is possible within reasonable geochemical limits. Accordingly, up to 1 per cent difference in V_P/V_S may be explained by compositional differences, for example, from fertile lherzolite to refractory harzburgite.

Svecofennian, Sveconorwegian and Caledonian units

Northeast of the main UMVB the high velocities and low V_P/V_S ratios extend down to depths of 250 km or more. We interpret these velocities in terms of a thick lithosphere with strong depletion in iron and fluids, thus with a high solidus temperature and high viscosity, thereby furthering longevity. The interpretation of thick lithosphere is in accordance with several previous works (Cotte *et al.* 2002; Gregersen *et al.* 2002, 2010; Hieronymus *et al.* 2007; Medhus *et al.* 2012a). We note that in southwestern Sweden this zone of thick lithosphere crosses the boundaries between Early Proterozoic Svecofennian units, the Trans-Scandinavian Igneous Belt and eastern Sveconorwegian units (compare with Fig. 1a).

In contrast to southern Sweden, low velocities and high V_P/V_S ratios are found in southern Norway, west of the UMVB. We interpret this region as having thinner lithosphere and higher temperatures. The upper mantle is likely to be less depleted, consistent with the observed higher V_P/V_S ratios, which lowers the 'resilience' of the LAB. We note that the change in V_P/V_S ratio is large compared to what is easily explained by a change in composition alone, thus implying higher upper-mantle temperatures, despite of relatively low heat flow. If the asthenosphere has developed partial melt here, it would imply even greater lowering of mainly V_S and hence a further increase in V_P/V_S ratio. Notably, the UMVB follows the eastern flank of the Late Carboniferous-Permian Oslo Graben, which has been suggested to have formed in a weakness zone between the eastern and western Sveconorwegian units (Pascal *et al.* 2002). The existence of a marked, old lithosphere boundary is supported by the results of a recent integrated lithospheric modelling study by Gradmann *et al.* (2013); see also discussion below.

Other studies have detected the particularly low *S* velocities below southern Norway using teleseismic tomography (Wawerzinek *et al.* 2013), surface wave tomography (Weidle & Maupin 2008; Maupin 2011; Köhler *et al.* 2012) and full waveform low-frequency

tomography (Rickers *et al.* 2013). Rickers *et al.* (2013) interpret this anomaly as being connected westwards to the 'Iceland - Jan Mayen plume system'. We find the centre of this low *S*-velocity anomaly close to the northern end of the Oslo Graben (marked b in Fig. 6), but we also identify higher relative *S*-velocities in southwestern Norway (a in Fig. 6), so if low velocities near the Oslo Graben connect at all, it looks more like a connection southward. Note that our checkerboard and recovery tests (Figs 9 and 15) show very good lateral resolution in this central part of the study area. This speaks against a single west-to-east protruding tongue of hot/slow material from the Atlantic side. Close scrutiny of Rickers *et al.* (2013: Fig. 6 at 160 km depth) shows that this study also detects the area of increased velocity in southwestern Norway. However, we do not rule out that flows in the asthenosphere can transport hotter and/or more fertile material over large distances, possibly leading to patchy low-velocity structure guided by, or generating, LAB topography, which may be what we see in southern Norway.

An obvious question is, if our results, emphasizing marked velocity anomalies in the upper mantle, may add new elements to the debate about the origin and nature of high topography of western Scandinavia including southern Norway (Caledonian as well as Sveconorwegian units, Fig. 1). A key point is the age of these anomalies. From previous studies on crustal thickness and gravity data (e.g. Balling 1980; Svenningsen *et al.* 2007; Ebbing *et al.* 2012), we find that the high topography of the Southern Scandes Mountains is isostatically compensated mainly by a thickened crust, thought to be largely of Caledonian age, resulting from continent-continent collision between Baltica and Laurentia (*cf.* introduction and Nielsen *et al.* 2009). However, reduced upper-mantle seismic velocities, thinned lithosphere and higher upper-mantle temperatures, as argued above, all point to also some reduction in density, which means that some buoyancy from both within the mantle lithosphere and below are likely (see also detailed discussions in Medhus *et al.* 2012a and Maupin *et al.* 2013). Our present results emphasize that most likely both temperature and compositional differences are needed to explain observed differences in seismic velocities between southern Norway and southern Sweden, dating back, at least in part, to Late Carboniferous-Permian (see discussion below), and perhaps even older tectonic processes as well. This indicates that such deep buoyancy and associated topography is more likely to have a relatively old origin. If some parts of the upper-mantle low-velocity anomalies connect to the North Atlantic, as discussed above, may a minor part of buoyancy and related topography be of a more recent nature.

Danish and North German Basins

In the region of the Danish and North German Basins, the shallower mantle zone, 100–200 km, is dominated by low relative *P* velocity and even lower relative *S*-velocity, so that the relative V_P/V_S anomaly is predominantly positive. This is consistent with a relatively shallow LAB as inferred from surface-wave analysis (Pedersen *et al.* 1994; Cotte *et al.* 2002; Köhler *et al.* 2015) and thermal modelling (Balling 1995; Norden *et al.* 2008). The low velocities and high relative V_P/V_S ratio suggest a less depleted mantle and higher temperatures compared with the adjacent thick shield lithosphere in southern Sweden. Several previous studies have interpreted these basins in terms of a complex sequence of rifting, stretching, and subsidence events (e.g. Van Wees *et al.* 2000; Frederiksen *et al.* 2001; McCann *et al.* 2006), with the Late Carboniferous, Permian and Triassic

magmatic and tectonic activity (Heeremans & Faleide 2004; Torsvik *et al.* 2008) as important episodes.

The enigmatic high-velocity body recovered in both *P* and *S* velocity between 200 and 300 km depth, centred near 10°E, 53°N (marked with f in Figs 5 and 6) also has a lower V_P/V_S ratio compared to the surrounding North German Basin. The upward smearing of this deeper high-velocity anomaly explains an apparent hole in the shallow North German low-velocity anomaly, however, still resolved and most clearly seen in the *P* model (Fig. 5 and at depth 50–200 km in Fig. 8). A very deep, local remnant of an old depleted lithospheric root in the Avalonian terrane, comparable to what is found under southern Sweden, could be an explanation for the high-velocity unit, but it would be very unlikely in the middle of a region subjected to Carboniferous–Permian–Triassic magmatism and rifting events. A more likely, but still somewhat speculative interpretation would be that the positive velocity anomaly is caused by an advected neutrally buoyant body, depleted in iron and fluids, implying a significantly higher solidus, relatively higher V_S, and lower V_P/V_S ratios.

The importance of the main UMVB and the relationship between the Danish Basin and this boundary are emphasized further in three vertical sections (Fig. 8). Section AA′ follows the direction of previous studies along the Tor array. The STZ is located at profile distance 650 km. The UMVB is very clearly expressed in all velocity indicators, and it seems to dip at about 45° under Sweden. Hieronymus *et al.* (2007) modelled this principal structure as a convective system southwest of the UMVB, bounded by high viscosity, long lived lithosphere northeast of the UMVB. The *P*- and the *S*-velocity models differ in detail regarding this dipping interface. We infer that the causes of velocity anomalies are both temperature (differences in heat flow and thermal structure, Balling 1995; Hieronymus *et al.* 2007; Norden *et al.* 2008) and the degree of depletion and possibly minor amounts of melt in a relatively shallow and well developed asthenosphere beneath the basins. These influence V_P and V_S differently, and do not need to follow the same subsurface distributions. So the different fine structure in V_P and V_S may be real.

Section BB′ runs from the Danish Basin across the STZ and the UMVB (at the 'Kattegat Bend') into the 'South Sweden Fast Zone'. The *P* velocity boundary is more diffuse, where *S* velocity contrasts stand strongly and V_P/V_S is more negative to the east compared with the lithosphere in profile AA′. We interpret this thick lithosphere beneath southwestern Sweden as being even more depleted than that found in profile AA′, implying even higher viscosity. This strong unit may have played an important role as control of the tectonic development of this area, as will be discussed below. The upper mantle below ∼300 km shows more normal V_P/V_S values.

Section CC′ runs north-south from the basins, across the STZ, into the Sveconorwegian units, across the Caledonian Front and into the highest topography of the Southern Scandes Mountains. Apart from a very nice delineation of the enigmatic high-velocity body deep under the North German Basin, this profile shows a surprisingly uniform low-velocity level with some deeper negative anomalies, particularly in V_S (depth 100–200 km at profile distance 500–600 km and depth c. 200 km at profile distance 900–1100 km). Most notably, we do not see much difference between the Danish Basin and the Southern Scandes Mountains (Sveconorwegian and Caledonian areas of high topography, Fig. 1a). An apparent clear separation of anomalies between these units around km 800 in section CC′ (in particular in the *S* model and the V_P/V_S), is due to the position of this profile passing close to the UMVB at its westernmost position (compare Figs 1a, 6 and 7).

The main UMVB and the Carboniferous-Permian magmatism

The similarity between southern Norway mantle and basin mantle to the south is remarkable. The indicated moderate thickness of the lithosphere under southern Norway is not easily explained considering the small differences in heat flow relative to the adjacent areas of southern Sweden (Balling 1995; Slagstad *et al.* 2009), but both temperature and compositional differences are likely to exist. Thus, in a recent integrated geophysical–petrological modelling study, Gradmann *et al.* (2013) emphasize that differences in the composition of the lithosphere between southern Norway and Sweden are needed to satisfy the gravity field and isostatically compensated topography. We see a north to south trend in the deepest minima in *S*-velocity (see intervals 100–300 km in Figs 5 and 6), running from just north of the Oslo Graben to central parts of the basins. Note that Rickers *et al.* (2013) also found relatively low *S*-velocity at levels 80–120 km, as well as deeper, under southern Norway. These features may be associated with a shallow LAB and related higher temperatures and lower average depletion at depths of 100–200 km. Such 'antiforms' in the LAB may be remnants of loss of lithosphere due to thermal erosion or convective instability at the climax of magmatism in the Late Carboniferous-Permian tectonic and magmatic activity.

The presence of such LAB antiforms today implies that the surviving lithosphere in Norway and Denmark has remained sufficiently resilient to convective/conductive smoothing of the LAB under the more 'normal' thermal and dynamic conditions after the Permian. This would attest to a degree of depletion which may even be as high as that we have mapped in southern Sweden outside the Fast Zone. The main UMVB may therefore be understood as representing the northeastern limit of 'lithosphere-asthenosphere attenuation' associated with the Late Carboniferous-Perminan tectonic and magmatic activity, the eastern boundary of which is outlined very close to the UMVB (*cf.* Heeremans & Faleide 2004). The fact that section BB′ in Fig. 8 shows the signature of a particularly high degree of lithospheric depletion and hence resilience right at the 'Kattegat Bend', where the UMVB turns northward, could indicate that this 'strong-point' played an important role in controlling the geometry of the Danish Basin and the Oslo Graben.

REFERENCES

Abramovitz, T. & Thybo, H., 2000. Seismic images of Caledonian collisional structures along MONA LISA profile 2 in the southeastern North Sea, *Tectonophysics,* **317,** 27–54.

Artemieva, I.M., 2009. The continental lithosphere: reconciling thermal, seismic, and petrologic data, *Lithos,* **109,** 23–46.

Artemieva, I.M., 2011. *The Lithosphere: An Interdisciplinary Approach,* Cambridge University Press, 794 pp.

Artemieva, I.M. & Thybo, H., 2013. EUNAseis: a seismic model for Moho and crustal structure in Europe, Greenland, and the North Atlantic region, *Tectonophysics,* **609,** 97–153.

Artemieva, I.M., Thybo, H. & Kaban, M., 2006. Deep Europe today: geophysical synthesis of the upper mantle structure and lithospheric processes over 3.5 Ga, in *European Lithosphere Dynamics,* pp. 11–41, eds Gee, D.G. & Stephenson, R.A., Geol. Soc. London Mem. 32.

Balling, N., 1980. The land uplift in Fennoscandia, gravity field anomalies and isostasy, in *Earth Rheology, Isostasy and Eustasy,* pp. 297–321, ed. Morner, N.-A., John Wiley & Sons.

Balling, N., 1995. Heat flow and thermal structure of the lithosphere across the Baltic Shield and northern Tornquist Zone, *Tectonophysics,* **244,** 13–50.

Balling, N., 2000. Deep seismic reflection evidence for ancient subduction and collision zones within the continental lithosphere of northwestern Europe, *Tectonophysics,* **329,** 269–300.

Bingen, B., Andersson, J., Söderlund, U. & Möller, C., 2008a. The Mesoproterozoic in the Nordic countries, *Episodes,* **31,** 29–34.

Bingen, B., Nordgulen, Ø. & Viola, G., 2008b. A four-phase model for the Sveconorwegian orogeny, SW Scandinavia, *Norw. J. Geology.,* **88,** 43–72.

Bogdanova, S.V., Bingen, B., Gorbatschev, R., Kheraskova, T.N., Kozlov, V.I., Puchkov, V.N. & Volozh Yu, A., 2008. The East European Craton (Baltica) before and during the assembly of Rodinia, *Precambrian Res.,* **160,** 23–45.

Bonow, J.M., Lidmar-Bergstrom, K., Japsen, P., Chalmers, J.A. & Green, P.F., 2007. Elevated erosion surfaces in central West Greenland and southern Norway: their significance in integrated studies of passive margin development, *Norw. J. Geology.,* **87,** 197–206.

Cammerano, F., Goes, S., Vacher, P. & Giardini, D., 2003. Inferring upper mantle temperatures from seismic velocities, *Phys. Earth planet. Inter.,* **138,** 197–222.

Chalmers, J.A., Green, P., Japsen, P. & Rasmussen, E.S., 2010. The Scandinavian mountains have not persisted since the Caledonian orogeny. A comment on Nielsen *et al.* (2009a), *J. Geodyn.,* **50,** 94–101.

Cocks, L.R.M. & Torsvik, T.H., 2006. European geography in a global context from the Vendian to the end of the Palaeozoic, in *European Lithosphere Dynamics,* pp. 83–95, eds Gee, D.G. & Stephenson, R.A., Geol. Soc. London Mem. 32.

Cotte, N., Pedersen, H.A. & TOR Working Group, 2002. Sharp contrast in lithospheric structure across the Sorgenfrei-Tornquist Zone as inferred by Rayleigh wave analysis of TOR1 project data, *Tectonophysics,* **360,** 75–88.

Dore, G.A., 1992. The base Tertiary surface of southern Norway and the northern North Sea, *Norw. J. Geol.,* **72,** 259–265.

Ebbing, J., England, R.W., Korja, T., Lauritsen, T., Olesen, O., Stratford, W. & Weidle, C., 2012. Structure of the Scandes lithosphere from surface to depth, *Tectonophysics,* **536,** 1–24.

England, R.W. & Ebbing, J., 2012. Crustal structure of central Norway and Sweden from integrated modelling of teleseismic receiver functions and the gravity anomaly, *Geophys. J. Int.,* **191,** 1–11.

EUGENO-S Working Group, 1988. Crustal structure and tectonic evolution of the transition between the Baltic Shield and the North German Caledonides (the EUGENO-S Project), *Tectonophysics,* **150,** 253–348.

Frederiksen, S., Nielsen, S.B. & Balling, N., 2001. A numerical dynamic model for the Norwegian-Danish Basin, *Tectonophysics,* **343,** 165–183.

Gee, D.G. & Stephenson, R.A., 2006. The European lithosphere: an introduction, in *European Lithosphere Dynamics,* pp. 1–9, eds Gee, D.G. & Stephenson, R.A., Geol. Soc. London Mem. 32.

Gradmann, S., Ebbing, J. & Fullea, J., 2013. Integrated geophysical modelling of a lateral transition zone in the lithospheric mantle under Norway and Sweden, *Geophys. J. Int.,* **194,** 1358–1373.

Green, P.F., Lidmar-Bergström, K., Japsen, P., Bonow, J.M. & Chalmers, J.A., 2013. Stratigraphic landscape analysis, thermochronology and the episodic development of elevated, passive continental margins, *Geological Survey of Denmark and Greenland Bulletin,* **30,** 150 pp.

Gregersen, S., Voss, P., Nielsen, L.V., Achauer, U., Busche, H., Rabbel, W. & Shomali, Z.H., 2010. Uniqueness of modeling results from teleseismic *P*-wave tomography in Project Tor, *Tectonophysics,* **481,** 99–107.

Gregersen, S., Voss, P. & TOR Working Group, 2002. Summary of project TOR: delineation of a stepwise, sharp, deep lithosphere transition across Germany–Denmark–Sweden, *Tectonophysics,* **360,** 61–73.

Heeremans, M. & Faleide, J.I., 2004. Late Carboniferous-Permian tectonics and magmatic activity in the Skagerrak, Kattegat and North Sea, in *Permo-Carboniferous Magmatism and Rifting in Europe,* pp. 157–179, eds Wilson, M., Neumann, E.R., Davies, G.R., Timmerman, M.J., Heeremans, M. & Larsen, B.T., Geol. Soc. London, Special Publication, 233.

Hejrani, B., Jacobsen, B.H. & Balling, N., 2014. Teleseismic tomography when stations follow profiles: pitfalls and remedies, *Seismol. Res. Lett.,* **85,** 997–1003.

Hieronymus, C.F., Shomali, Z.H. & Pedersen, L.B., 2007. A dynamical model for generating sharp seismic velocity contrasts underneath continents: application to the Sorgrenfrei-Tornquist Zone, *Earth planet. Sci. Lett.,* **262,** 77–91.

Iwasaki, T., Sellevoll, M.A., Kanazawa, T., Veggeland, T. & Shimamura, H., 1994. Seismic refraction crustal study along the Sognefjord, south-west Norway, employing ocean-bottom seismometers, *Geophys. J. Int.,* **119,** 791–808.

Jakovlev, A., Bushenkova, N.A., Koulakov, I.Y. & Dobretsov, N.L., 2012. Structure of the upper mantle in the Circum-Arctic region from regional seismic tomography, *Russ. Geol. Geophys.,* **53,** 963–971.

Japsen, P. & Chalmers, J.A., 2000. Neogene uplift and tectonics around the north Atlantic: overview, *Glob. Planet. Change.,* **24,** 165–173.

Jones, A.G., Plomerova, J., Korja, T., Sodoudi, F. & Spakman, W., 2010. Europe from the bottom up: a statistical examination of central and northern European lithosphere-asthenosphere boundary from comparing seismological and electromagnetic observations, *Lithos,* **120,** 14–29.

Kennett, B.L.N. & Engdahl, E.R., 1991. Travel times for global earthquake location and phase identification, *Geophys. J. Int.,* **105,** 429–465.

Kennett, B.L.N. & Gudmundsson, O., 1996. Ellipticity corrections for seismic phases, *Geophys. J. Int.,* **127,** 40–48.

Kind, R. *et al.*, 2013. Scandinavia: a former Tibet?, *Geochem. Geophys. Geosyst.,* **14,** 4479–4487.

Köhler, A., Maupin, V. & Balling, N., 2015. Surface wave tomography across the Sorgenfrei-Tornquist Zone, SW Scandinavia, using ambient noise and earthquake data, *Geophys. J. Int.,* in press.

Köhler, A., Weidle, C. & Maupin, V., 2012. Crustal and uppermost mantle structure of southern Norway: results from surface wave analysis of ambient noise and earthquake data, *Geophs. J. Int.,* **191,** 1441–1456.

Kolstrup, M., Hung, S.-H. & Maupin, V., 2015. Multiscale, finite-frequency *P* and *S* tomography of the upper mantle in the southwestern Fennoscandian Shield, *Geophys. J. Int.,* **202,** 190–218.

Lee, C.T.A., 2003. Compositional variation of density and seismic velocities in natural peridotites at STP conditions: implications for seismic imaging of compositional heterogeneities in the upper mantle, *J. geophys. Res.,* **108,** 2441, doi:10.1029/2003JB002413.

Lidmar-Bergström, K., Ollier, C.D. & Sulebak, J.R., 2000. Landforms and uplift history of southern Norway, *Glob. Planet. Change,* **24,** 211–231.

Maupin, V., 2011. Upper mantle structure in southern Norway from beam-forming of Rayleigh wave data presenting multipathing, *Geophys. J. Int.,* **185,** 985–1002.

Maupin, V. *et al.*, 2013. The deep structure of the Scandes and its relation to tectonic history and present-day topography, *Tectonophysics,* **602,** 15–37.

McCann, T. *et al.*, 2006. Post-Variscan (end Carboniferous-Early Permian), basin evolution in Western and Central Europe, in *European Lithosphere Dynamics,* pp. 355–388, eds Gee, D.G. & Stephenson, R.A., Geol. Soc. Lond. Mem. 32.

Medhus, A.B., Balling, N., Jacobsen, B.H., Weidle, C., England, R.W., Kind, R., Thybo, H. & Voss, P., 2012a. Upper-mantle structure beneath the Southern Scandes Mountains and the Northern Tornquist Zone revealed by *P*-wave traveltime tomography, *Geophys. J. Int.,* **189,** 1315–1334.

Medhus, A.B., Jacobsen, B.H. & Balling, N., 2012b. Bias problems in existing teleseismic travel time databases: ignore or repair?, *Seismol. Res. Lett.,* **83,** 1030–1037.

Nielsen, S.B. *et al.*, 2009. The evolution of western Scandinavian topography: a review of Neogene uplift versus the ICE (isostasy-climate-erosion) hypothesis, *J. Geodyn.,* **47,** 72–95.

Nielsen, S.B., Clausen, O.R., Jacobsen, B.H., Thomsen, E., Huuse, M., Gallagher, K., Balling, N. & Egholm, D.L., 2010. The ICE hypothesis stands: how the dogma of late Cenozoic tectonic uplift can no longer be sustained in the light of data and physical laws, *J. Geodyn.,* **50,** 102–111.

Norden, B., Forster, A. & Balling, N., 2008. Heat flow and lithospheric thermal regime in the Northeast German Basin, *Tectonophysics,* **460,** 215–229.

Olsson, S., Roberts, R.G. & Bodvarsson, R., 2008. Moho depth variation in the Baltic Shield from analysis of converted waves, *Geologiska Föreningen i Stockholm Förhandlingar,* **130,** 113–122.

Pascal, C., van Wijk, J., Cloetingh, S.A.P.L. & Davies, G.R., 2002. Effect of lithosphere thickness heterogeneities in controlling rift localization: numerical modelling of the Oslo Graben, *Geophys. Res. Lett.,* **29,** 1355, doi:10.1029/2001GL014354.

Pedersen, H.A., Campillo, M. & Balling, N., 1994. Changes in the lithospheric structure across the Sorgenfrei-Tornquist Zone inferred from dispersion of Rayleigh waves, *Earth planet. Sci. Lett.,* **128,** 37–46.

Rickers, F., Fichtner, A. & Trampert, J., 2013. The Iceland–Jan Mayen plume system and its impact on mantle dynamics in the North Atlantic region: evidence from full-waveform inversion, *Earth planet. Sci. Lett.,* **367,** 39–51.

Roberts, D., 2003. The Scandinavian Caledonides: event chronology, palaeogeographic setting and likely modern analogues, *Tectonophysics,* **365,** 283–299.

Sandrin, A. & Thybo, H., 2008. Deep seismic investigation of crustal extensional structures in the Danish Basin along the ESTRID-2 profile, *Geophys. J. Int.,* **173,** 623–641.

Scheck-Wenderoth, M. & Lamarche, J., 2005. Crustal memory and basin evolution in the Central European Basin System–new insights from a 3D structural model, *Tectonophysics,* **397,** 143–165.

Schutt, D.L. & Lesher, C.E., 2010. Compositional trends among Kaapvaal Craton garnet peridotite xenoliths and their effects on seismic velocity and density, *Earth planet. Sci. Lett.,* **300,** 367–373.

Slagstad, T., Balling, N., Elvebakk, H., Midttomme, K., Olesen, O., Olsen, L. & Pascal, C., 2009. Heat-flow measurements in late Palaeoproterozoic to Permian geological provinces in south and central Norway and a new heat-flow map of Fennoscandia and Norwegian-Greenland sea, *Tectonophysics,* **473,** 341–361.

Stratford, W. & Thybo, H., 2011. Seismic structure and composition of the crust beneath the southern Scandes, Norway, *Tectonophysics,* **502,** 364–382.

Stratford, W., Thybo, H., Faleide, J.I., Olesen, O. & Tryggvason, A., 2009. New Moho Map for onshore southern Norway, *Geophys. J. Int.,* **178,** 1755–1765.

Stuevold, L.M. & Eldholm, O., 1996. Cenozoic uplift of Fennoscandia inferred from a study of the mid-Norwegian margin, *Glob. Planet. Change,* **12,** 359–386.

Svenningsen, L., Balling, N., Jacobsen, B.H., Kind, R., Wylegalla, K. & Schweitzer, J., 2007. Crustal root beneath the highlands of southern Norway resolved by teleseismic receiver functions, *Geophys. J. Int.,* **170,** 1129–1138.

Tesauro, M., Kaban, M.K. & Cloetingh, S.A.P.L., 2008. EuCRUST-07: a new reference model for the European crust, *Geophys. Res. Lett.,* **35,** L05313, doi:10.1029/2007GL032244.

Torsvik, T.H. & Rehnström, E.F., 2003. The Tornquist Sea and Baltica-Avalonia docking, *Tectonophysics,* **362,** 67–82.

Torsvik, T.H., Smethurst, M.A., Bruke, K. & Steinberger, B., 2008. Long term stability in deep mantle structure: evidence from the ∼300 Ma Skagerrak-Centered Large Igneous Province (the SCLIP), *Earth planet. Sci. Lett.,* **267,** 444–452.

Van Wees, J.D. *et al.*, 2000. On the origin of the Southern Permian Basin, Central Europe, *Mar. Pet. Geol.,* **17,** 43–59.

Voss, P.H., Mosegaard, K., Gregersen, S. & TOR Working Group, 2006. The Tornquist Zone, a north east inclining lithospheric transition at the south western margin of the Baltic Shield: revealed through a non-linear teleseismic tomographic inversion, *Tectonophysics,* **416,** 151–166.

Wawerzinek, B., Ritter, J.R.R. & Roy, C., 2013. New constraints on the 3-D shear wave velocity structure of the upper mantle underneath Southern Scandinavia revealed from non-linear tomography, *Tectonophysics,* **602,** 38–54.

Weidle, C. & Maupin, V., 2008. An upper-mantle *S*-wave velocity model for Northern Europe from Love and Rayleigh group velocities, *Geophys. J. Int.,* **175,** 1154–1168.

Weidle, C. *et al.*, 2010. MAGNUS — a seismological broadband experiment to resolve crustal and upper mantle structure beneath the Southern Scandes Mountains in Norway, *Seismol. Res. Lett.,* **81,** 76–84.

Zhu, H., Bozdağ, E.D. & Tromp, J., 2012. Structure of the European upper mantle revealed by adjoint tomography, *Nat. Geosci.,* **5,** 493–498.

Zielhuis, A. & Nolet, G., 1994. Deep seismic expression of an ancient plate boundary in Europe, *Science,* **265,** 79–81.